The Use of the Source Reconstruction Method for Antenna Characterization

by

Chaitanya Narendra

A Thesis submitted to the Faculty of Graduate Studies of
The University of Manitoba
in partial fulfilment of the requirements of the degree of

MASTER OF SCIENCE

Department of Electrical and Computer Engineering
University of Manitoba
Winnipeg, Manitoba, Canada

"Study hard what interests you the most in the most undisciplined, irreverent and original manner possible."

Richard Feynman

Abstract

by Chaitanya Narendra

This thesis studies the use of the Source Reconstruction Method (SRM) to characterize antennas. The SRM calculates equivalent sources/currents on an arbitrarily shaped reconstruction surface to represent the original antenna. This is done by enforcing that the original antenna and equivalent currents radiate the same field at user selected measurement locations. These equivalent currents spatially characterize the original antenna because they can be used in direct radiation problems to obtain field estimates anywhere outside the reconstruction surface, including the far-field.

First a spherical SRM algorithm is implemented and the diagnostic capabilities of the SRM are also synthetically shown through an example with an array of elementary dipoles. It is then shown that the SRM compares well to pre-existing commercial antenna software over different frequencies and can also be used successfully with a partial dataset. It is demonstrated that the equivalent currents can also provide meaningful information with experimental data.

Next the hierarchical matrix framework is studied in conjunction with the SRM to decrease the algorithm's memory requirement and increase the speed of execution. It is shown that it is beneficial to use the hierarchical matrix framework with the SRM when using Love's condition or with measured data on a surface very close to the reconstruction surface.

The SRM is then used to obtain incident field estimates in microwave imaging systems. Using a 2D transverse magnetic framework, we show that even with the limited data available in typical microwave tomography setups the SRM can produce incident field estimates in the imaging domain. These estimates are then used along with an MR-GNI algorithm to image synthetic and experimental objects with uncalibrated measured data.

Acknowledgements

I would first like to thank my advisors Dr. Puyan Mojabi and Dr. Ian Jeffrey for all the help and inspiration that they have given me throughout my time in the M.Sc. program. They always try to go above and beyond and will always have my appreciation and friendship.

Thank you to Dr. Sherif Sherif and Dr. Derek Krepski for taking the time to help me improve my thesis by advising on my M.Sc. examination committee.

I would also like to express my gratitude to the University of Manitoba (UM) Electromagnetic Imaging Laboratory, UM Antenna Laboratory and NovAtel Inc. for all the resources that they provided for my research.

I'd like to thank my friend Trevor Brown for his help with the development of the spherical source reconstruction method code for this research and for always keeping our office environment enjoyable.

Finally, I would like to thank the University of Manitoba GETS program, and Natural Sciences and Engineering Research Council for providing funding for my research.

Contents

List of Figures

List of Tables

Important Abbreviations

ACA	**A**daptive **C**ross **A**pproximation
AUT	**A**ntenna **U**nder **T**est
CATR	**C**ompact **A**ntenna **T**est **R**ange
CG	**C**onjugate **G**radient
CGLS	**C**onjugate **G**radient **L**east **S**quares
$\mathcal{H}$-matrix	**H**ierarchical **m**atrix
ME	**M**odal **E**xpansion
MLFMM	**M**ulti-**L**evel **F**ast **M**ultipole **M**ethod
MWI	**M**icro**w**ave **I**maging
MWT	**M**icro**w**ave **T**omography
OI	**O**bject of **I**nterest
RWG	**R**ao-**W**ilton-**G**lisson (basis functions)
SRM	**S**ource **R**econstruction **M**ethod
SVD	**S**ingular**V**alue **D**ecomposition
2D	**2 D**imensional
3D	**3 D**imensional

Important Symbols

λ	Wavelength
D	Largest dimension of the antenna
$\mathcal{S}'$	Reconstruction Surface
$\mathcal{S}'$	Measurement Surface
$\mathcal{S}_{\text{love}}$	Love's Surface
$\mathcal{D}$	Imaging Domain
$\vec{r}$, $\vec{r}'$	Observation position vector and source position vector, respectively
k_0	Wavenumber of free space
k_b	Wavenumber of the background medium
η_0	Free space impedance
$\vec{E}$	Total electric field
$\vec{E}_J$	Electric current contribution to the electric field
$\vec{E}_M$	Magnetic current contribution to the electric field
$\vec{J}$	Electric current density (may be referred to as electric current)
$\vec{M}$	Magnetic current density (may be referred to magnetic current)
ω	Angular frequency
$(.)^H$	Hermitian Operator

To my parents and sister...

Chapter 1

Introduction

Broadly speaking, this thesis is focused in the area of near-field antenna characterization. The purpose of this chapter is to refresh the reader about this area and to describe one important antenna characterization method, namely, the Source Reconstruction Method (SRM). The scope, general outline and contributions of this work are also presented.

1.1 Antenna Characterization

Antenna characterization is the act of describing an antenna under test (AUT). Antennas can be characterized in terms of circuit properties (*e.g.* impedance, voltage across the terminals etc.) and spatial properties (*e.g.* far-field pattern, near-field distribution, directivity etc.). In this thesis we consider the task of spatial characterization (*i.e* describing the antenna's electromagnetic fields), which is important for antenna fabrication, optimization and verification. For example, if an antenna is being designed to send and receive a signal from almost all directions, it will require a specific omni-directional far-field pattern. Once this antenna is designed and fabricated, it must be tested to see

if the original design specifications were met, otherwise it will not perform as expected for its intended application.

When characterizing an AUT the most fundamental spatial property is its surface current distribution. If the surface current distribution of the AUT is known, any other spatial property can be inferred. The main advantage of the method studied in this thesis (SRM) is that it inherently makes available a current distribution that can be used to fully characterize the AUT, which is not true of the traditional methods.

Antenna characterization is performed through the use of antenna measurement systems referred to as antenna ranges. These measurement systems can be separated into two main groups: far-field ranges, and near-field ranges. Far-field ranges work by measuring the AUT's far-field pattern directly, while near-field ranges use near-field (electromagnetic) measurements as input to algorithms that can estimate the AUT's far-field or provide other properties. Far-field and near-field ranges are briefly described in the following subsections and an overview of the basic concept of near-field range algorithms is presented.

1.1.1 Near-field and Far-field of an Antenna

Before going on, it may be beneficial to remind the reader about the far-field and near-field zones of an AUT. The electromagnetic field distribution of an AUT can be broken into different regions in space. The region closest to the AUT is the near-field region followed by the far-field region. The distance to the far-field is usually defined as the larger quantity of either 10λ or $\frac{2D^2}{\lambda}$ where λ is the wavelength of operation and D is the largest dimension of the AUT. Most antenna's are designed to operate in the far-field

region because the electromagnetic field pattern varies very little with distance. The region up until the far-field is referred to as the near-field of the AUT.

1.1.2 Far-field Antenna Ranges

Far-field ranges can either be indoor or outdoor systems. Common outdoor far-field ranges include the elevated range and slant range, while the compact antenna test range (CATR) is an example of an indoor far-field range [2, 3]. An advantage of outdoor far-field ranges is that, due to the availability of space, they can easily measure the far-field of large and/or low frequency AUTs (see Section 1.1.1). Furthermore, outdoor far-field ranges are useful when the AUT needs to be tested in a specific outdoor environment (*e.g.* an antenna on a ship).

The disadvantage of outdoor far-field ranges is that they require a considerable amount of space in a location that does not have much electromagnetic noise or unwanted signals. Furthermore, because of the size of the equipment involved (antenna mounting towers) it can be difficult to change the apparatus for different tests. Reflections of the AUT's field from the ground and any nearby scatterers should also be managed carefully with outdoor ranges if only the free space far-field pattern is intended for measurement.

CATRs are meant to be used indoors within anechoic chambers [4]. These measurement systems use special transforming devices such as parabolic reflectors to try and simulate far-field conditions within a smaller physical test environment [5]. CATRs are used indoors so measurements can be performed in a controlled environment. It is also much easier to change the CATR setup to perform different experiments. Finally, because CATRs work by interrogating the AUT with (approximate) uniform plane waves, radar cross section measurements [6] are easy to perform.

The convenience of an indoor far-field measurement range is somewhat offset by the cost of the required indoor apparatus. Anechoic chambers are expensive due to the absorbers that are needed to simulate a free space environment within the anechoic chamber (they are needed to limit reflections from the anechoic chamber structure). The price of these absorbers also increases if high power antennas are being used, because they must be specially designed to dissipate the energy. Furthermore the size of the absorbers is related to the frequency band that they will be used with. Consequently, the lower the frequency of operation, the larger (and more expensive) the absorbers one needs. This leads to expensive anechoic chamber designs if low frequency antennas are to be used. Note that the disadvantages listed in this paragraph apply to all indoor ranges that require anechoic chambers.

CATRs also have limitations due to the method in which they attempt to create far-fields using reflectors. The far-field/uniform plane wave conditions that are created by CATRs are only acceptable in a certain region of space in the anechoic chamber [5]. This region is referred to as the quiet zone, and it is usually about one-third the size of the reflector that is used, thus limiting the size of the AUT that can be characterized. CATR reflectors also need to be fabricated very carefully to avoid defects because this directly affects the uniform plane wave quality of the quiet zone [5]. Consequently, these reflectors are an expensive piece of the CATR apparatus.

1.1.3 Near-field Antenna Ranges

Near-field antenna characterization is performed using algorithms capable of predicting properties of the AUT using measurements of the AUT's electromagnetic field taken in the near-field region [7]. This characterization is mainly accomplished through the use of near-field antenna measurement systems such as the planar near-field range, cylindrical

near-field range, and spherical near-field range. Near-field measurement systems are mainly designed to work indoors within anechoic chambers.

The main advantage of near-field measurement systems is that because measurements are performed in the AUT's near-field region (usually within 3λ - 5λ), the overall measurement system is compact and convenient as opposed to most far-field measurement systems. Near-field systems do not require a quiet zone in the vicinity of the AUT because far-field conditions do not need to be simulated, this means that no expensive reflectors are needed. Consequently near-field systems are inexpensive compared to most other antenna ranges.

Near-field ranges work by employing near-field to far-field transformation algorithms whereas far-field ranges measure the far-field pattern of the AUT directly. Therefore, the compactness of near-field ranges comes at the cost of algorithmic complexity.

1.1.4 Near-field Range Algorithms

Near-field antenna systems typically calculate the far-field of an AUT through the use of modal expansion (ME) algorithms [8]. These ME algorithms use electromagnetic near-field measurements as input and transform these measurements to estimate the far-field of the AUT.

The basic principle of ME algorithms is to decompose near-field measurements into known wave modes, and then propagate these known waves to the appropriate locations to obtain the field. As an example, consider a plane of near-field measurements in front of an AUT. We can decompose this plane of measurements into plane waves using Fourier transforms. Once we have represented the near-field measurements as a summation of

plane waves, we can propagate these waves to the far-field to obtain our estimate. A similar procedure can be done for cylindrical and spherical waves.

ME algorithms are used extensively in practice, but they do have certain disadvantages. The main disadvantage of ME algorithms is that they are not flexible when it comes to acquisition/measurement domains. These domains must be canonical surfaces [9] with co-located tangential field measurements which brings forth the need for additional assumptions rather than using just the original measurement data.

1.2 Brief Introduction to the Source Reconstruction Method

The SRM attempts to calculate a set of equivalent sources/currents on a reconstruction surface $\mathcal{S}'$ in such a way that they produce the same electromagnetic field as the original AUT at the measurement locations on the measurement surface $\mathcal{S}$. These sources can then be used with the appropriate Green's function to estimate the electromagnetic field anywhere outside $\mathcal{S}'$. A more detailed explanation of the SRM formulation is explained in Chapter 2.

The SRM has many advantages over the conventional ME methods. For example, the SRM can be used with any arbitrary measurement surface $\mathcal{S}$, which allows more flexibility in the way antenna measurement systems are developed and used, an example is shown in Section 3.2.2. The SRM does *not* require a strict data (co-located tangential components) set like the ME methods and so no assumptions have to be made about missing data like in the case of the planar and cylindrical near-field to far-field transformations. SRM allows the incorporation prior information about the AUT when solving for the equivalent currents, and ME does not. Finally, since the SRM requires calculation of equivalent currents, these currents can be used for antenna diagnostic purposes

(see Section 3.2.1). This information can be very useful to engineers who must verify the AUT once it is fabricated.

The main disadvantage of the SRM is that it requires the solution of an electromagnetic inverse source problem to calculate the equivalent currents before these currents can be used to acquire the field outside $\mathcal{S}'$, whereas in the ME methods, the far-field is calculated directly from the measured data. Consequently, the SRM carries more computational expense compared to ME. Finally, due to the fact that the electromagnetic inverse source problem that must be solved is ill-posed [10], a regularization scheme or method of picking an appropriate solution (see Section 2.2.2), is required. These issues can be circumvented to a degree, and the many benefits of the SRM qualify it for further study.

1.3 Brief Source Reconstruction Method Literature Review

The SRM was first introduced in [11–13] as an equivalent magnetic currents method that served as an alternative to ME for obtaining the far-field antenna pattern of the AUT with the advantages that: it could provide a set of equivalent currents characterizing the AUT, and it did not have to assume information about measurement data like the planar and cylindrical ME methods. In this seminal work, SRM examples were shown with planar measurement domains and an example with probe compensation (removing the effect of the probe when measurements are taken [7]) was given. The general increase in computational requirements of this then newly discovered approach over ME was also observed. In [14, 15], methods of obtaining the far-field from near-field measurements on arbitrary measurement surface geometries were shown. This was done with equivalent magnetic currents [14], and electric currents [15]. The planar ME

and planar magnetic current SRM was compared in [16], and it was shown that the SRM was able to provide more accurate results for a finite measurement plane for a tradeoff of computational cost. The SRM was also used in [17] in a method that can be used to obtain the magnetic current distribution of an AUT with phaseless near-field measurements. This phaseless method can be used with measurement domains of arbitrary shape. These phaseless measurement techniques are useful at very high frequencies (millimetre wave) for which phase is difficult to measure accurately. The magnetic current SRM with two planar reconstruction surfaces was used to characterize commercial antennas in [18], and in [19] the SRM was used to obtain the currents on axially symmetric radomes. The reconstruction of equivalent currents over 3D arbitrary surfaces was outlined in [1] and [20] where in the latter paper the achievable resolution of the reconstructed currents was improved through the use of Rao-Wilton-Glisson basis functions. Different mathematical formulations for the SRM were compared in [21, 22] which is beneficial with regards to choosing the appropriate formulation for specific applications. The spherical wave expansion (spherical ME) and the SRM was compared in [9] and it was shown that although the SRM had higher computational cost, it could provide diagnostic capabilities that the spherical wave expansion could not. The far-field patterns computed by both methods were comparable. A simple probe correction method for the SRM was introduced in [23] where the effect of the probe was accounted for as a weighting function included in the SRM integral equations.

The high computational cost of the SRM has also been addressed in the literature by making use of state of the art acceleration methods such a adaptive cross approximation (ACA) in [24], and multi-level fast multipole method (MLFMM) in [25, 26], where in [26] full probe correction was demonstrated with MLFMM. A parallel implementation of the SRM utilizing graphics processors was also recently shown in [27].

In summary, SRM has been demonstrated to be generally more capable than ME and current research has addressed the issue of the increased computational cost.

1.4 Contributions of Thesis Work

In this section the contributions that were made as part of this thesis are listed. Separate subsections show the papers and conference presentations that resulted from this work.

The SRM was implemented in both C++ and MATLAB code for spherical measurement domain geometries and was tested with synthetic and experimental data. This SRM implementation was compared to a commercially available modal expansion algorithm available at the University of Manitoba Antenna Laboratory.

The hierarchical matrix framework was investigated for use with the spherical SRM with the goal of improving memory requirements and speed of execution. It was shown that it is advantageous to use this framework if Love's condition is utilized, but if it not it is better to compress the full operator. To the best of knowledge, a similar study had not previously been conducted.

The SRM was utilized to characterize the transmitting antennas in a microwave imaging setup. More specifically the SRM was employed to estimate incident field distributions in the imaging domain for use with microwave imaging inverse scattering algorithms. It was shown in a 2D transverse magnetic microwave tomography framework with synthetic and experimental data that this SRM method can be used to produce meaningful images of objects without the use of incident or scattered field calibration techniques.

1.4.1 Journal Papers

C. Narendra, I. Jeffrey, and P. Mojabi, "Using the Source Reconstruction Method to Model Incident Fields in Microwave Tomography," *IEEE Antennas Wireless Propag. Lett.*, IEEE Early Access, 2016.

1.4.2 Conference Papers/Presentations

C. Narendra, I. Jeffrey, and P. Mojabi, "On the use of the source reconstruction method to estimate incident field distributions in microwave imaging," in *IEEE International Symposium on Antennas and Propagation/USNC-URSI National Radio Science Meeting*, Vancouver, BC, 2015.

C. Narendra, I. Jeffrey, T. Brown, J. Aronsson, and P. Mojabi, "Hierarchical Matrix Acceleration of the Source Reconstruction Method for Antenna Measurements," in *IEEE International Symposium on Antennas and Propagation/USNC-URSI National Radio Science Meeting*, Fajardo, Puerto Rico, 2016.

1.4.3 Other

T. Brown, **C. Narendra**, I. Jeffrey, and P. Mojabi, "NSERC Engage Project: The Source Reconstruction Method for Near-Field Antenna Measurements," Technical Report submitted to NovAtel Inc., Calgary, AB, 2015, unpublished, pp. 24.

1.5 Scope of Thesis

The scope or extent of the work undertaken in this thesis is described in this section.

1.5.1 Source Reconstruction Method for Spherical Measurement Domains

The SRM was implemented for use with spherical measurement domains. Antenna measurement systems with spherical measurement domains are advantageous for the following reasons:

1. In general, more electromagnetic data is collected around the AUT compared to planar systems and cylindrical systems. Therefore the AUT can be characterized more accurately.

2. Commercial near-field antenna measurement systems use ME algorithms for near-field to far-field transformations. These ME algorithms need to make assumptions about the measured data for cylindrical and planar measurement domains and so the spherical systems are the most accurate [9, 16].

Due to the reasons above, an SRM algorithm for spherical measurement domains was chosen as the focus of this work. This algorithm could then be compared to spherical ME algorithms (no truncation error resulting from assumptions about measurement data), and would be able to use more information from around the AUT. A final motivating factor for limiting the scope to spherical near-field measurement systems was the availability of experimental spherical measurement data.

It is important to note that SRM algorithms are, in general, applicable to arbitrary measurement domains, and the developed implementation herein can be adopted accordingly for other systems in future work. Experimentally verifying such an implementation of the SRM for a more arbitrary measurement surface would have taken more time and

resources (*i.e* need to obtain or build a measurement system that obtains measurement data for different measurement domains geometries) and was thus not considered further.

1.5.2 Source Reconstruction Method for Microwave Tomography

This thesis also deals with the antenna characterization required in microwave tomography (MWT). In MWT, transmitting antennas irradiate the object being imaged, and these antennas need to be represented by appropriate numerical models within the imaging algorithm. In this thesis, we propose to use the SRM to characterize these antennas in MWT systems. This characterization can then be incorporated within the imaging algorithm. There are many different types of MWT systems that have been reported in literature, including 2D and 3D systems. Our investigation of using SRM within imaging algorithms was limited to 2D TM MWT system for 3 main reasons:

1. This is the most common microwave tomography system seen in literature.
2. There is a better balance of knowns to unknowns for these types of systems (see [28]).
3. Experimental data from a 2D TM system was available.

Although we choose to work with such a system, there is nothing fundamentally limiting the SRM from being used with other types of microwave imaging systems, and a study of the practical aspects of using SRM in other systems could make for interesting future work.

1.6 Thesis Outline

The current chapter presented an introduction, briefly explaining antenna characterization and the SRM. The contributions and scope of this thesis were also presented.

Chapter 2 will explain the general theory and mathematical framework of SRM. The inversion of the resulting ill-posed problem will also be discussed.

Chapter 3 goes into more detail about the specific spherical SRM implementation. We also present synthetic and experimental results showing the main advantages and disadvantages of the SRM. The issue of the SRM computational cost is addressed through the implementation of the hierarchical matrix framework. We investigate when it is beneficial to use the hierarchical matrix framework and when it is more beneficial to compress the full discrete operator.

We show how the SRM can be used to characterize transmitting antennas in MWT inverse scattering algorithms in Chapter 4. It is shown both synthetically and experimentally that if the SRM is used to estimate the incident fields in MWT, we can invert raw (uncalibrated) data to obtain accurate images of an object of interest.

The conclusion of this work presented in Chapter 5 along with possible future research avenues.

Chapter 2

Source Reconstruction Method Theory

This chapter presents the general SRM theory, then describes the SRM mathematical framework including: forward problem formulation, solving the electromagnetic inverse source problem, and regularization.

2.1 Source Reconstruction Method Process

The SRM is founded on the electromagnetic equivalence principle [29], which allows one to replace the original problem in which a radiator is producing some electromagnetic field with an equivalent one where that original radiator is replaced with a set of equivalent currents on an arbitrarily shaped, reconstruction surface $\mathcal{S}'$. The surface $\mathcal{S}'$ encloses the original radiator that it replaced and produces the same field as the original radiator outside $\mathcal{S}'$, while the field inside $\mathcal{S}'$ can be arbitrary as shown in Figure 2.1. The discontinuity in the fields inside and outside $\mathcal{S}'$ necessitates the presence of the (equivalent)

surface currents $\vec{J}$ and $\vec{M}$ as shown by the boundary condition equations derived from Maxwell's equations in Figure 2.1.

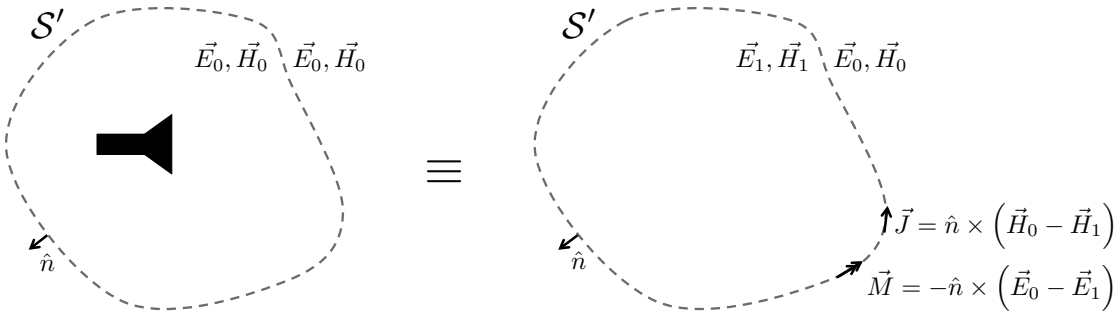

Figure 2.1: The equivalence principle. The original problem [left] can be replaced by an equivalent one [right] where the original radiator is replaced by a set of equivalent currents on $\mathcal{S}'$.

In the context of antenna measurements, the same process is applied to characterize the AUT. Measurements are taken over a measurement surface $\mathcal{S}$, and an inverse source problem is solved using the measured field values to obtain the equivalent currents on $\mathcal{S}'$. As mentioned earlier, this is done with the intention that the reconstructed equivalent currents will produce the same field values at the measurement locations on $\mathcal{S}$ as the original AUT. Once the currents are calculated, they can be used in a direct radiation problem to obtain field estimates anywhere outside $\mathcal{S}'$, including the far-field region[1]. This process is illustrated in Figure 2.2 for a spherical near-field antenna measurement system. Spherical systems make use of spherical measurement domains $\mathcal{S}$, but in the interest of formatting $\mathcal{S}$ is shown as a hemisphere in Figure 2.2. In general, $\mathcal{S}$ and $\mathcal{S}'$ can be arbitrarily shaped when using the SRM.

It is also important to note that when using the SRM the best results may be achieved when $\mathcal{S}'$ is a closed surface (as required by the equivalence principle), and all tangential components over a closed $\mathcal{S}$ are measured (as required by the uniqueness theorem [29] to identify a unique source). However, the SRM does not require that the aforementioned

[1]If the field is calculated between $\mathcal{S}'$ and $\mathcal{S}$ then it is not guaranteed to be accurate because of the absence of evanescent (non-propagating) wave data on $\mathcal{S}$.

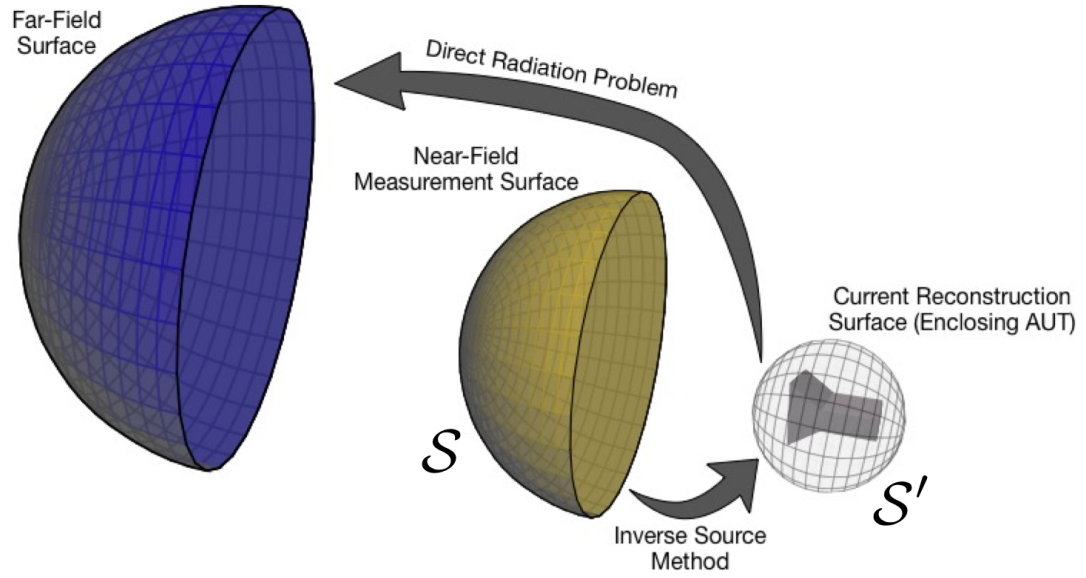

Figure 2.2: SRM applied to spherical near-field antenna measurements. In actual spherical measurement systems $\mathcal{S}$ completely encloses the AUT. This process can be generalized to any arbitrarily shaped $\mathcal{S}$ and $\mathcal{S}'$. This figure is based on one from [1].

conditions are followed in the mathematical formulation, and accurate results may still be achieved as shown in Chapter 4. The SRM mathematical formulation is explained in detail in the next section.

2.2 Source Reconstruction Method Mathematical Framework

This section describes the mathematical framework of the SRM, including how the forward problem is formulated, how the inverse problem is solved, and the need for regularization techniques. Broadly speaking, the forward problem is concerned with finding the electromagnetic field from a given set of known currents; *e.g.*, finding field values on $\mathcal{S}$ from known sources on $\mathcal{S}'$, see Figure 2.2. On the other hand, the inverse

source problem is concerned with finding sources from measured electromagnetic fields; *e.g.*, finding (reconstructing) the sources on $\mathcal{S}'$ from the known field values on $\mathcal{S}$.

2.2.1 Forward Problem

In order to obtain the electric field ($\vec{E}(\vec{r})$) at a given receiver/measurement location ($\vec{r}$) from a set of currents at specific source locations ($\vec{J}(\vec{r}\,')$ and $\vec{M}(\vec{r}\,')$), the well known electric field integral equations can be used.

$$\begin{aligned} \vec{E}_J(\vec{r}) &= -jk_0\eta_0 \int_{\mathcal{S}'} \left[\vec{J}(\vec{r}\,') + \frac{1}{k_0^2}\nabla\nabla'\cdot\vec{J}(\vec{r}\,')\right] g(\vec{r},\vec{r}\,')d\mathcal{S}' \\ \vec{E}_M(\vec{r}) &= -\nabla\times\int_{\mathcal{S}'} \vec{M}(\vec{r}\,')\cdot g(\vec{r},\vec{r}\,')d\mathcal{S}' \end{aligned} \tag{2.1}$$

In (2.1), $\vec{E}_J(\vec{r})$ and $\vec{E}_M(\vec{r})$ are the electric field contributions from the electric current density $\vec{J}(\vec{r}\,')$ and magnetic current density $\vec{M}(\vec{r}\,')$, respectively. Furthermore, k_0 is the free space wavenumber, η_0 is the impedance of free space, $g(\vec{r},\vec{r}\,')$ is the Green's function of free space, and ∇' indicates taking surface derivatives over the prime coordinates (source coordinates).

The 3D Green's function of free space is

$$g(\vec{r},\vec{r}\,') = \frac{e^{-jk_0|\vec{r}-\vec{r}\,'|}}{4\pi|\vec{r}-\vec{r}\,'|}. \tag{2.2}$$

To obtain the total electric field at a point $\vec{r}$ one would have to add the contributions of the electric and magnetic field integral equations.

$$\vec{E}(\vec{r}) = \vec{E}_J(\vec{r}) + \vec{E}_M(\vec{r}) \tag{2.3}$$

The magnetic field integral equations, with magnetic field measured values for the SRM can be used as well as (2.1). These equations can be obtained from (2.1) through the principle of duality [29]. It should also be mentioned that all the equations above can be generalized to backgrounds other than free-space, but the free-space equations are used most often in antenna measurement applications.

When using (2.1), there is only a discrete finite set of measured data at certain measurement locations and source locations that will contain equivalent currents. Therefore, (2.1) is discretized and eventually reduces to a linear matrix equation of the form

$$\mathbf{A}\mathbf{x} = \mathbf{b} \tag{2.4}$$

where in (2.4), $\mathbf{A}$ is a discrete operator matrix that maps source currents to measured values through the Green's function, $\mathbf{b}$ is a vector of measured field values, and $\mathbf{x}$ is a vector representing the unknown equivalent currents that must be calculated. In other words, the operator $\mathbf{A}$ maps the current sources on domain $\mathcal{S}'$, see Figure 2.2, to field values on domain $\mathcal{S}$. It should be noted that (2.1) can be discretized in different ways depending on the problem and basis functions used to represent the unknown equivalent current values, and this process will be shown in more detail in later chapters.

Solving (2.4) for $\mathbf{x}$ is referred to as solving a linear inverse source problem, and this is the main challenge associated with the SRM.

2.2.2 Source Reconstruction Method Inversion

Solving (2.4) for **x** is not a straight forward process for two main reasons:

1. The problem is ill-posed.

2. The associated discrete linear problem is ill-conditioned.

The problem is ill-posed [10] because it is not guaranteed that the calculated solution (set of currents) is unique. The electric field integral equations that we are trying to solve take the form of Fredholm integral equations of the first kind [30] where the unknown function (in our case the current densities) only appears under the integral. Simplified, we can write the general form of such equations as

$$b(\vec{r}) = \int_{\mathcal{S}'} A(\vec{r}, \vec{r}\,')x(\vec{r}\,')d\vec{r}\,' \tag{2.5}$$

where (2.5) is the continuous form of (2.4), *i.e.* $b(\vec{r})$ is the measured data, $A(\vec{r}, \vec{r}\,')$ is the operator mapping source points to measurement points, $x(\vec{r}\,')$ is the source, $\vec{r} \in \mathcal{S}$, and $\vec{r}\,' \in \mathcal{S}'$. Now consider a case where we have the following situation

$$0 = \int_{\mathcal{S}'} A(\vec{r}, \vec{r}\,')x_{null}(\vec{r}\,')d\vec{r}\,' \tag{2.6}$$

If a non-trivial solution exists to (2.6), in other words, if there is a solution $x_{null}(\vec{r}\,')$ that is not zero everywhere that produces zero at all the measurement locations $\vec{r} \in \mathcal{S}$ (known as nonradiating sources [31]), then we could have an infinite set of solutions

$$x_{full}(\vec{r}\,') = x_{sol}(\vec{r}\,') + zx_{null}(\vec{r}\,') \tag{2.7}$$

that would produce the same data at the measurement locations ($x_{sol}(\vec{r}')$ is a radiating solution and z is an arbitrary constant) as shown below.

$$
\begin{aligned}
&\text{if } b_0(\vec{r}) = \int_{\mathcal{S}'} A(\vec{r},\vec{r}')x_{sol}(\vec{r}')d\vec{r}' \text{ where } \vec{r} \in \mathcal{S} \\
&b_{full}(\vec{r}) = \int_{\mathcal{S}'} A(\vec{r},\vec{r}')x_{full}(\vec{r}')d\vec{r}' \\
&b_{full}(\vec{r}) = \int_{\mathcal{S}'} A(\vec{r},\vec{r}')(x_{sol}(\vec{r}') + zx_{null}(\vec{r}'))d\vec{r}' \\
&b_{full}(\vec{r}) = \int_{\mathcal{S}'} A(\vec{r},\vec{r}')(x_{sol}(\vec{r}')d\vec{r}' + z\int_{\mathcal{S}'} A(\vec{r},\vec{r}')x_{null}(\vec{r}'))d\vec{r}' \\
&b_0(\vec{r}) = \int_{\mathcal{S}'} A(\vec{r},\vec{r}')x_{sol}(\vec{r}')d\vec{r}' + 0
\end{aligned}
\tag{2.8}
$$

Note that the set of all solutions satisfying (2.6) is referred to as the null space of the operator. Due to the finite set of measurement field values that the calculated set of equivalent currents must produce, there is no implicit constraint on the solution outside the measured field values. There are infinite solutions (current distributions) that can produce the measured field values on $\mathcal{S}$, but may produce different field values elsewhere. This is one justification of the existence of the null space of the operator. This type of linear inverse source problems always pose a null space [30]. The problem of ill-posedness is solved with regularization techniques (picking an appropriate solution) and is discussed in the Section 2.2.2.3.

When solving these types problems the issue of solution existence may also arise. Mathematically speaking, we are worried about the accuracy of the mapping operator from sources to fields. In our case, the background medium dictates the Green's function that is used, but other obstructions (*e.g.* anechoic chamber structure, measurement equipment) are not taken into consideration. Consequently, one can not expect that **A** can

exactly represent the true physical situation. However this is a minor issue and even using the Green's function of free space, accurate results can be achieved. Physically speaking, a solution always exists because there is always an antenna that created our measured field.

SRM problems are also ill-conditioned due to the operator structure derived from (2.1). Because these equations take the form of Fredholm integral equations of the first kind, matrices formed by discretizing them have singular values approaching zero [32]. Consequently, the condition number of the discrete operator matrix (the ratio of the largest singular value to the smallest singular value) will be very large resulting in an ill-conditioned matrix. If matrices are ill-conditioned, numerical inversion/solution techniques can incur significant error.

This inherent instability due to the decaying of singular values is best explained using the concept of the singular value decomposition (SVD). Through the SVD, $\mathbf{A}$ in (2.4), which represents our discretized operator matrix, can be expanded as a matrix of right singular vectors $\mathbf{U}$, a diagonal matrix (usually rectangular) of singular values $\mathbf{\Sigma}$, and a matrix of left singular vectors $\mathbf{V}$. Let us assume that $\mathbf{A}$ is size $n \times m$. Then taking the economical SVD we have

$$\begin{aligned} \mathbf{Ax} &= \mathbf{b} \\ \mathbf{U\Sigma V^H x} &= \mathbf{b} \end{aligned} \tag{2.9}$$

Using the properties that $\mathbf{U}^H\mathbf{U} = \mathbf{I}$, $\mathbf{V}^H\mathbf{V} = \mathbf{I}$ ($\mathbf{I}$ is the identity matrix), and $\mathbf{\Sigma}^{-1}$ is a new diagonal matrix where the new diagonal are the reciprocals of the original matrix we can write the solution $\mathbf{x}$ in terms of the singular vectors and singular values.

$$\mathbf{x} = \sum_{i=1}^{min(n,m)} \frac{\mathbf{u_i^H b}}{\sigma_\mathbf{i}} \mathbf{v_i} \tag{2.10}$$

In (2.10), $\mathbf{u_i}$ and $\mathbf{v_i}$ are the columns of $\mathbf{U}$ and $\mathbf{V}$, respectively, while $\sigma_\mathbf{i}$ are the singular values on the diagonal of $\mathbf{\Sigma}$.

Furthermore, incorporating the measurement error in our measurement vector $\mathbf{b}$, we can write

$$\mathbf{b} = \mathbf{b_{exact}} + \mathbf{e} \tag{2.11}$$

where in (2.11), $\mathbf{b_{exact}}$ represents the ideal measurement vector with no errors, and $\mathbf{e}$ represents the vector of incurred error. Using (2.11), we can re-write (2.10).

$$\mathbf{x} = \sum_{\mathbf{i}=1}^{min(n,m)} \frac{\mathbf{u_i^H b_{exact}}}{\sigma_\mathbf{i}} \mathbf{v_i} + \frac{\mathbf{u_i^H e}}{\sigma_\mathbf{i}} \mathbf{v_i} \tag{2.12}$$

Focusing on the first term $\frac{\mathbf{u_i^H b_{exact}}}{\sigma_\mathbf{i}} \mathbf{v_i}$, we note that the singular values $\sigma_\mathbf{i}$ monotonically decrease with the same or slower rate (with respect to the index $\mathbf{i}$) as $|\mathbf{u_i}^H \mathbf{b_{exact}}|$, so this term is stable. However, the same can not be said for the second term $\frac{\mathbf{u_i^H e}}{\sigma_\mathbf{i}} \mathbf{v_i}$, and after some index $\mathbf{i}$ determined by the error $\mathbf{e}$, this term starts to get larger, thereby dominating the solution [32]. We want the solution to be weighted more with the true solution b_{exact} and not the error. This instability can be avoided by using some form of regularization so that not all of the $\mathbf{i}$ singular values and vectors are used to calculate the solution [32].

2.2.2.1 Inversion Methods

There are many different types of inversion methods for linear inverse source problems, but they can be divided into two main categories [32]:

1. Direct Methods
2. Iterative Methods

In this context, direct methods refer to inverse source solution techniques that use direct factorizations of the discrete operator matrix $\mathbf{A}$ to arrive at a physically meaningful solution, while the iterative techniques do not use factorizations.

Some common factorizations are the QR decomposition, or the SVD. Direct methods are disadvantageous in that the factorizations of $\mathbf{A}$ are generally computationally expensive and memory intensive. For example, if $\mathbf{A}$ was a square matrix of size n, then the SVD and QR decomposition of $\mathbf{A}$ have a computational complexity $\mathcal{O}(n^3)$. Therefore, if working with large matrices, direct methods are not usually used.

In contrast to direct methods, iterative methods do not involve factorizing $\mathbf{A}$, and instead involve iteratively calculating the solution $\mathbf{x}$ by using $\mathbf{A}$ in matrix-vector products [32]. These methods are more suitable when $\mathbf{A}$ is very large because (again assuming $\mathbf{A}$ is square and of size n) matrix-vector products have a computational complexity of $\mathcal{O}(n^2)$ for dense matrices, and if k iterations are performed, then we have a total computational complexity of $\mathcal{O}(kn^2)$. This is advantageous because due to the need for regularization, typically (see Section 2.2.2.3) $k << n$. Therefore in this thesis, we focus on iterative solution/regularization methods of the linear inverse problem as in the antenna measurement applications we deal with, the size of $\mathbf{A}$ is very large.

2.2.2.2 Conjugate Gradient Least Squares

The conjugate gradient (CG) method is an iterative technique that is good for solving problems in the form of (2.4). As previously mentioned, it is beneficial to use this technique when the number of iterations is less than the size of the operator matrix dimensions. CG can only be used to solve (2.4) if the discrete operator matrix $\mathbf{A}$ is symmetric, and positive definite.

In our case, we know that $\mathbf{A}$ is not symmetric and positive definite, in fact, it is often overdetermined (rectangular) in antenna measurements. Therefore, we use the conjugate gradient least squares (CGLS) algorithm instead. CGLS attempts to solve the following minimization problem:

$$\underset{\mathbf{x}}{\operatorname{argmin}} \|\mathbf{A}\mathbf{x} - \mathbf{b}\|_2^2 \tag{2.13}$$

In (2.13), we are minimizing the L^2 norm. The problem shown in (2.13) can solved by expanding the norm, taking the derivative and setting it equal to zero to obtain

$$\mathbf{A}^H\mathbf{A}\mathbf{x} = \mathbf{A}^H\mathbf{b} \tag{2.14}$$

which are called the normal equations. Solving (2.14) gives us the least squares solution $\mathbf{x}$. In other words, calculating $\mathbf{x}$ in this way would give the solution (equivalent current distribution) that would produce the field with the smallest sum of the squared errors at the measurement locations [33]. Now (2.14) can be solved with CG. This process is referred to as CGLS, because we are implicitly using CG with the normal equations to obtain the least squares solution. It is very important that this is done implicitly *i.e.*

$\mathbf{A}^H\mathbf{A}$ is never explicitly formed because this would square the condition number of the operator and make our problem more ill-conditioned [34]. Note that if $\mathbf{A}$ was originally symmetric and positive definite, then using CG, we would also obtain the solution to (2.13) except in this case, it would be the exact solution.

It is intuitive to explain the steps of CGLS as a minimization problem. The global minimum of our search space is the solution to (2.13) and contains our least squares solution $\mathbf{x}$. Therefore, the goal is to start somewhere on this search space, and navigate to the global minimum. The first step is to pick an initial guess $\mathbf{x_0}$. In this work, the initial guess was assumed to be the zero vector. This means we start at some point on the paraboloidal work space [33]. Now we must choose what direction to move.

In CGLS, the direction is some combination of the negative gradient at the previous iteration with the negative gradient calculated at the current iteration. At the first iteration, we set the direction to the first residual. The residual, in this case, is $\mathbf{A}^H(\mathbf{b} - \mathbf{A}\mathbf{x_0})$. This residual is used because as can be inferred from (2.13), (2.14), and their relationship, it is the negative gradient of the functional (2.13). Since the direction of the gradient always points in the direction of greatest increase, if we take some combination of the negative gradients, we know that we will be getting closer to the global minima. So the first step is

$$\mathbf{d}_0 = \mathbf{r}_0 \tag{2.15}$$

where $\mathbf{d}_0$ is the initial direction, and the right hand side is the initial residual.

Once we have calculated the initial direction, we must decide how far we should travel along that direction. This is done by finding the minimum of the functional along this

direction. This calculation reduces to

$$\alpha_i = \frac{\mathbf{r}_i^H \mathbf{r}_i}{\mathbf{d}_i^H \mathbf{A}\mathbf{d}_i}. \tag{2.16}$$

In (2.16), i refers to the iteration number, and α is the 'distance' we are travelling. Once this is done, we can calculate our new estimate for $\mathbf{x}$.

$$\mathbf{x}_{i+1} = \mathbf{x}_i + \alpha_i \mathbf{d}_i \tag{2.17}$$

Next, we must update the residual. The residual can be updated efficiently by using the following formula:

$$\mathbf{r}_{i+1} = \mathbf{r}_i - \alpha_i \mathbf{A}^H \mathbf{A}\mathbf{d}_i \tag{2.18}$$

In (2.18), $\mathbf{r}$ refers to the residual. Using this formula to update the residual is more efficient because we re-use the $\mathbf{A}\mathbf{d}_i$ term that we had to use to calculate α_i, thereby saving multiplication operations per iteration.

The last steps involve picking a new direction to keep moving toward the global minimum. As mentioned earlier, this is a combination of the residual calculated from the current iteration, and the previous search direction. There are many ways to weight the previous search direction, however, these different methods only affect the performance of the algorithm significantly if the cost functional we are minimizing is non-quadratic [35] which is not the case here. Therefore all the weighting methods should show similar performance. In our case we chose the Fletcher-Reeves method:

$$\beta_{i+1} = \frac{\mathbf{r}_{i+1}^H \mathbf{r}_{i+1}}{\mathbf{r}_i^H \mathbf{r}_i} \tag{2.19}$$

In (2.19), β is the weighting factor for the CGLS direction update. Once this is calculated, we finally update our direction and perform the previously shown steps (iteratively) as necessary.

$$\mathbf{d}_{i+1} = \mathbf{r}_{i+1} + \beta_{i+1}\mathbf{d}_i \tag{2.20}$$

The algorithm to perform CGLS is quite simple, and was implemented based on [36]. As previously mentioned, in most cases we do not want to continue the CGLS iterations until we reach the global minima because this solution would contain inaccuracies caused by error in the measured field values (see Section 2.2.2). Therefore regularization is needed, and an appropriate regularization method based on the CGLS algorithm itself is explained in the next section.

2.2.2.3 Conjugate Gradient Least Squares Regularization

Regularization of the inverse source problem using CGLS involves truncating the CGLS iterations appropriately. One method of deciding where to stop the CGLS iterations is the L-curve method [32]. This is a graphical technique, wherein the norm of the solution is graphed against the norm of the residual of $\mathbf{Ax} = \mathbf{b}$ *i.e.*, the x-axis is $\|\mathbf{Ax_i} - \mathbf{b}\|_2$ and the y-axis is $\|\mathbf{x_i}\|_2$. The curve takes the shape of an L, and shows the trade-off in minimizing the residual and minimizing the size of the solution as you go through more iterations ($\mathbf{i}$). If iterations progress too far, the size of the solution $\mathbf{x}$ can grow very large. This is undesired as it is caused by the solution trying to fit error in the

measured values as shown earlier in the chapter with SVD (the SVD and CGLS are related [34]) analysis. Therefore the iteration corresponding to the corner point of the L-curve is usually chosen to balance the size of the residual and size of the solution. A great illustration of a typical L-curve is given in [32]. It should also be noted that the iteration corresponding to the corner point is usually less than the actual rank of the full operator matrix $\mathbf{A}$, making it beneficial to use CGLS for inversion of large systems.

It should be noted that due to the low-pass nature of the Green's function [32] with respect to distance from the source, even without using an L-curve to pick specific equivalent current distributions, accurate far-field results can be obtained. In this case, one can monitor the normalized residual at each iteration, and terminate the CGLS algorithm when the normalized residual goes below some user selected value or starts to stagnate. This is advantageous in antenna measurement applications when plotting an entire L-curve is too time consuming, and only the far-field is desired.

Chapter 3

Source Reconstruction Method for Antenna Measurements

This chapter describes the implementation of a spherical SRM algorithm. The algorithm was developed and tested with synthetic and experimental data. It was also compared with an existing commercial modal expansion (ME) algorithm at the University of Manitoba Antenna Laboratory. The spherical algorithm is explained, and the synthetic and experimental results are shown and discussed. The SRM has shown great promise in antenna measurements (see Section 1.3) and in this chapter we consolidate this evidence with our own results.

3.1 Spherical Source Reconstruction Method Algorithm

In spherical antenna measurement schemes, the measured data are the tangential electric field components over a spherical measurement surface $\mathcal{S}$ as shown in Figure 2.2[1]. We

[1]The tangential magnetic field data or a combination of tangential magnetic and electric data field may also be used. For a spherical system, the $\hat{\theta}$ and $\hat{\varphi}$ components are the tangential components on $\mathcal{S}$.

then apply an SRM algorithm for spherical surfaces to this data to obtain equivalent currents on a reconstruction surface $\mathcal{S}'$. The unknown equivalent currents must be mathematically represented in some way. We chose to represent these currents using the Rao-Wilton-Glisson (RWG) basis functions [37].

3.1.1 Rao-Wilton-Glisson Basis Functions

RWG basis functions were chosen to represent the equivalent currents on $\mathcal{S}'$. RWG basis functions have the advantage of being defined on triangular patches which can be used to mesh any geometrical shape. This allows flexibility in choosing the shape of $\mathcal{S}'$ in antenna measurement applications. RWG basis functions are not prone to the build up of line or point charges on $\mathcal{S}'$. This is because RWG basis functions enforce continuity of the normal component of current across the edge of adjacent triangular elements [37]. In this way, the reconstructed equivalent currents behave more Maxwellian because they imply that the fields on $\mathcal{S}'$ are continuous in free space just like the fields produced by the AUT.

To implement the RWG basis, we associate an unknown coefficient with each unique edge (see n^{th} edge in Figure 3.1) of the reconstruction mesh.

$$\vec{J}(\vec{r}\,') \simeq \sum_{n=1}^{N} I_n f_n(\vec{r}\,') \tag{3.1}$$

In (3.1) $\vec{J}$ is the current, I_n is the coefficient associated with each edge, $f_n(\vec{r}\,')$ is the RWG basis function at a certain location on $\mathcal{S}'$, and N is the number of non-boundary edges. To calculate the total current, we sum the product of the coefficients and basis functions for all edges except the boundary edges. At the boundaries, the coefficients

must be zero to preserve current continuity. It should be noted that from an inverse problem point of view, we would be trying to solve for the coefficients I_n. The actual RWG basis functions can be described as follows:

$$f_n(\vec{r}\,') = \begin{cases} \frac{l_n}{2A_n^+}\vec{\rho}^{\,+} & \vec{r}\,' \text{ in } T_n^+ \\ \frac{l_n}{2A_n^-}\vec{\rho}^{\,-} & \vec{r}\,' \text{ in } T_n^- \\ 0 & \text{otherwise} \end{cases} \tag{3.2}$$

In (3.2), the + and − signs denote the two adjacent faces of the triangles connected to the n^{th} edge. The flow of current is always from the + triangle to the − triangle. The length of the n^{th} edge is l_n, the area of the appropriate positive or negative triangle is represented with A_n^+. The actual triangles associated with the n^{th} edge are denoted by T_n^+ and T_n^- and the choice of which triangle is the positive and negative element is arbitrary. The vector $\vec{\rho}^{\,+}$ is calculated by subtracting the free vertex (vertex of the triangle not associated with the n^{th} edge) from $\vec{r}\,'$ if $\vec{r}\,'$ is in T_n^+. Therefore $\vec{\rho}^{\,+}$ always points towards the n^{th} edge. On the other hand, $\vec{\rho}^{\,-}$ is calculated by subtracting $\vec{r}\,'$ from the free vertex of the − patch if $\vec{r}\,'$ is in T_n^-. All of this is illustrated in Figure 3.1.

3.1.2 Mesh Generation

In order to generate the triangular patches over all the necessary surfaces (*e.g.* $\mathcal{S}$ and $\mathcal{S}'$) we used a open source mesh generator software called Gmsh [38]. This is free software available under the GNU General Public License (GPL) with an exception for later versions to trouble-free linking with other libraries. Gmsh was written in standard C++ and uses the BLAS and LAPACK libraries for most of the linear algebra to uphold the original development goal of being fast, light and user friendly.

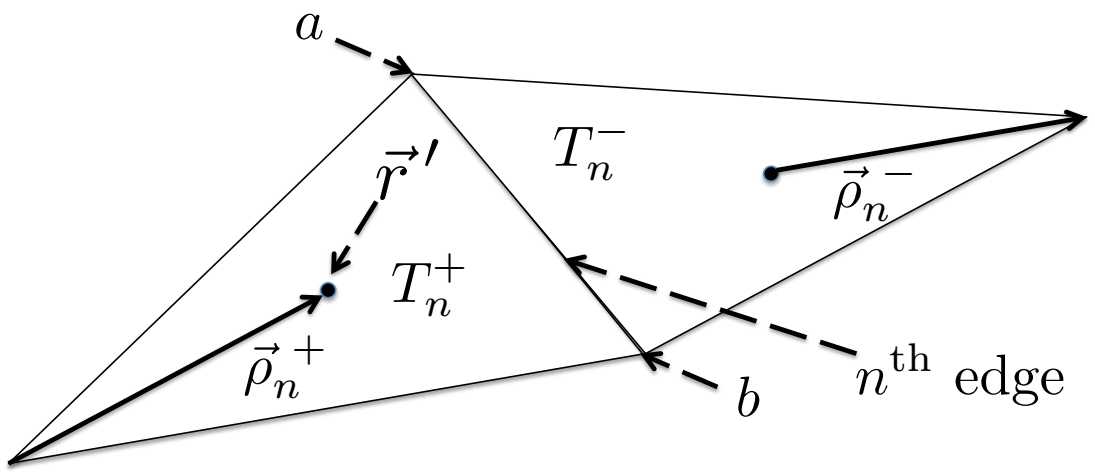

Figure 3.1: The n^{th} edge when using RWG basis functions. The distance from a to b is l_n. T_n^+ and T_n^- are the positive and negative elements, respectively. Both $\vec{\rho}_n^{\,+}$ and $\vec{\rho}_n^{\,-}$ examples are shown and are represented by solid arrows. The points/dots are example source points $\vec{r}\,'$ in the triangular elements.

3.1.3 3D Source Reconstruction Method Problem Formulation

Once we have chosen a method to represent our currents, we discretize (2.1) so that the vector of unknowns $\mathbf{x}$ corresponds to the RWG coefficients, and the measured values $\mathbf{b}$ are the tangential components of the electric field over a spherical measurement domain $\mathcal{S}$. All the derivatives in (2.1) are calculated analytically, *i.e.* no approximations are needed here. The integrals over the individual triangular elements are approximated using a fifth order, seven point Gaussian Quadrature rule [39]. It should be noted that the implementation of this algorithm is capable of incorporating other Quadrature rules.

After the discretization of (2.1), the overall matrix equation can be illustrated as

$$\underbrace{\begin{bmatrix} \mathbf{A}_{\mathbf{j}\theta} & \mathbf{A}_{\mathbf{m}\theta} \\ \mathbf{A}_{\mathbf{j}\varphi} & \mathbf{A}_{\mathbf{m}\varphi} \end{bmatrix}}_{\mathbf{A}} \underbrace{\begin{bmatrix} \mathbf{J_{eq}} \\ \mathbf{M_{eq}} \end{bmatrix}}_{\mathbf{x}} = \underbrace{\begin{bmatrix} \mathbf{E}_\theta \\ \mathbf{E}_\varphi \end{bmatrix}}_{\mathbf{b}}. \tag{3.3}$$

In (3.3) $\mathbf{A}_{\mathbf{j}\theta}$ and $\mathbf{A}_{\mathbf{m}\theta}$ are sub-matrices that represent the mapping of the electric and

magnetic edge coefficients to the $\hat{\theta}$ polarization of the electric field. Similarly, $\mathbf{A_{j\varphi}}$ and $\mathbf{A_{m\varphi}}$ are sub-matrices that represent the mapping of the electric and magnetic edge coefficients to the $\hat{\varphi}$ polarization of the electric field where $\hat{\theta}$ and $\hat{\varphi}$ are unit vectors in the spherical coordinate system. Also, $\mathbf{J_{eq}}$ and $\mathbf{M_{eq}}$ are vectors of unknown edge coefficients that would allow us represent the electric and magnetic current densities with the RWG basis on $\mathcal{S}'$, respectively. The vectors $\mathbf{E}_\theta$ and $\mathbf{E}_\varphi$ are the measured tangential components of the electric field on $\mathcal{S}$, where $\mathbf{E}_\theta$ contains the $\hat{\theta}$ components of the electric field and $\mathbf{E}_\varphi$ contains the $\hat{\varphi}$ components.

In (3.3) $\mathbf{A}$ and $\mathbf{b}$ are known. Now we must solve the inverse problem to obtain the unknown vector $\mathbf{x}$.

3.1.4 3D Source Reconstruction Method Inversion

To invert the system of equations shown in (3.3), we follow the same process outlined in Section 2.2.2.2. In this process, $\mathbf{A}$ and $\mathbf{b}$ are those vectors given in (3.3), and we will end up solving for $\mathbf{x}$ in the same equation. We did not always use the L-curve to pick an appropriate truncation iteration. For some of these tests, we were mainly concerned with the far-field produced by the solution $\mathbf{x}$, and as mentioned earlier, this pattern is not affected greatly by forgoing the use of the L-curve.

3.1.5 Love's Condition

It was mentioned in Section 2.1 that the field inside the reconstruction surface $\mathcal{S}'$ can be arbitrary. If this is the case, then the surface currents calculated on $\mathcal{S}'$ may not have much use for antenna engineers/designers (see Figure 2.1). In order to get the field outside $\mathcal{S}'$ to relate directly to the reconstructed currents, we can use Love's condition. If

the reconstructed currents relate directly to the field, they are easier to use for diagnostic purposes because antenna engineers/designers are more likely to know the expected field close to their AUTs.

Love's condition is implemented by creating a recessed mesh (with respect to $\mathcal{S}'$) and enforcing that the tangential components of the field on this surface (which we will call $\mathcal{S}_{\text{love}}$) are zero. This is a condition that the reconstructed equivalent currents must follow. This can be viewed as adding synthetic measurement data to the problem *i.e* adding zeros to the **b** vector. This in turn would necessitate that the field inside $\mathcal{S}'$ is zero as well, and consequently the reconstructed equivalent currents should relate directly to the field outside $\mathcal{S}'$. This is summarized in Figure 3.2. Practically, since we have a finite set of points on $\mathcal{S}_{\text{love}}$, and we are not infinitely close to $\mathcal{S}'$ so the actual method is an approximation to enforcing Love's condition exactly. However, the calculated equivalent currents do relate to the external field more closely [22].

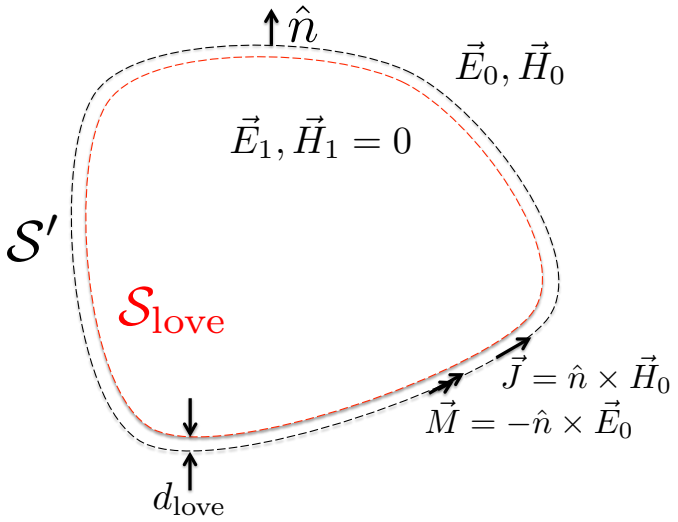

Figure 3.2: Diagram summarizing Love's condition. The surface $\mathcal{S}_{\text{love}}$ is recessed from $\mathcal{S}'$. The distance between them is d_{love} everywhere. We can see that if Love's condition is enforced, the boundary conditions imply that the calculated currents on $\mathcal{S}'$ relate directly to the field outside $\mathcal{S}'$.

The distance between $\mathcal{S}_{\text{love}}$ and $\mathcal{S}'$ is usually small ($\leq \frac{\lambda}{10}$ where λ is the wavelength) to

uphold the criterion of the surface current boundary condition equations. Furthermore, it is evident that since we are effectively adding synthetic measurement data, the size of our matrix equation will become much larger. In fact, it is recommended that we use more points on Love's surface than edges on $\mathcal{S}'$ in order to obtain good results [21]. If Love's condition is used, then (3.3) expands to

$$\underbrace{\begin{bmatrix} \mathbf{A}_{\mathbf{j}\theta} & \mathbf{A}_{\mathbf{m}\theta} \\ \mathbf{A}_{\mathbf{j}\varphi} & \mathbf{A}_{\mathbf{m}\varphi} \\ \mathbf{A}^{\text{love}}_{\mathbf{j}\theta} & \mathbf{A}^{\text{love}}_{\mathbf{m}\theta} \\ \mathbf{A}^{\text{love}}_{\mathbf{j}\varphi} & \mathbf{A}^{\text{love}}_{\mathbf{m}\varphi} \end{bmatrix}}_{\mathbf{A}} \underbrace{\begin{bmatrix} \mathbf{J}_{\mathbf{eq}} \\ \mathbf{M}_{\mathbf{eq}} \end{bmatrix}}_{\mathbf{x}} = \underbrace{\begin{bmatrix} \mathbf{E}_\theta \\ \mathbf{E}_\varphi \\ \mathbf{0} \\ \mathbf{0} \end{bmatrix}}_{\mathbf{b}}. \tag{3.4}$$

It is easy to see that (3.4) is a much bigger problem than (3.3). The amount of rows of $\mathbf{A}$ will increase by about the twice the size of edges (unknown coefficients), and b will grow by the same amount. This is due to the different $\hat{\theta}$ and $\hat{\varphi}$ polarizations. Note that zero vectors ($\mathbf{0}$) have been added to $\mathbf{b}$. These zero vectors are the synthetic measurement data on Love's surface and correspond to the enforced zero tangential fields of $\mathbf{E}_\theta$ and $\mathbf{E}_\varphi$. If the reconstruction surface $\mathcal{S}'$ is not a sphere, then (3.4) can be generalized by realizing that instead of mapping the sources on $\mathcal{S}'$ to the $\hat{\theta}$ and $\hat{\varphi}$ components of the recessed Love's surface, we will instead map these sources to the tangential components on this Love's surface.

3.1.6 Scaling the Source Reconstruction Method Operator Matrix

The relative sizes (with respect to magnitude) of the blocks of the discrete operator matrix for mapping the electric current density and magnetic current density to tangential fields are not the same. In fact, the sub-matrices of the discrete operator matrix

that are related the magnetic current density have elements that are generally larger in magnitude. This creates a problem when using CGLS to find $\mathbf{x}$. In fact, we find that the magnetic currents are more accurate than the electric currents. We speculate that this is because in CGLS, we are trying to minimize the functional shown in (2.13). So with every iteration of CGLS, the algorithm can make more progress if it changes the part of the solution which most affects the minimization of that functional, and this of course corresponds to the magnetic currents. In order to solve this problem, we normalize the magnetic parts of the discrete operator matrices by 377 (which we have found is the approximate ratio of the magnitude difference between $\mathbf{A_j}$ and $\mathbf{A_m}$ by comparing their norms). So the linear matrix equation that is really being solved is

$$\underbrace{\begin{bmatrix} \mathbf{A_{j\theta}} & \frac{1}{377}\mathbf{A_{m\theta}} \\ \mathbf{A_{j\varphi}} & \frac{1}{377}\mathbf{A_{m\varphi}} \\ \mathbf{A}^{\text{love}}_{\mathbf{j}\theta} & \frac{1}{377}\mathbf{A}^{\text{love}}_{\mathbf{m}\theta} \\ \mathbf{A}^{\text{love}}_{\mathbf{j}\varphi} & \frac{1}{377}\mathbf{A}^{\text{love}}_{\mathbf{m}\varphi} \end{bmatrix}}_{\mathbf{A}} \underbrace{\begin{bmatrix} \mathbf{J_{eq}} \\ \tilde{\mathbf{M}}_{\mathbf{eq}} \end{bmatrix}}_{\mathbf{x}} = \underbrace{\begin{bmatrix} \mathbf{E}_\theta \\ \mathbf{E}_\varphi \\ \mathbf{0} \\ \mathbf{0} \end{bmatrix}}_{\mathbf{b}}. \tag{3.5}$$

If Love's condition is not being used, then the Love's part of $\mathbf{A}$ is not present. Note that if we use CGLS to solve this, the algorithm seems to be better balanced with respect to solving for the correct electric and magnetic currents. However, the magnetic currents that we calculate ($\tilde{M}_{eq}$) using this technique are too large in magnitude (they are are larger to compensate for the normalized operators), therefore we divide the magnetic currents by 377 to obtain the correct current magnitude, *i.e.* $M_{eq} = \frac{\tilde{M}_{eq}}{377}$.

3.2 Spherical Source Reconstruction Method Algorithm Results

This section displays the results obtained from the implemented spherical SRM algorithm. Tests are shown for synthetic and experimentally collected near-field data. The SRM algorithm is compared with a commercially available ME algorithm to show the SRM's applicability for antenna measurements. Finally equivalent current distributions are shown, and their usability for antenna diagnostics is discussed.

3.2.1 Synthetic Tests

Tests were executed with synthetically created near-field data on the measurement surface $\mathcal{S}$. We first ran tests by simulating a single infinitesimal dipole. The field due to an infinitesimal dipole can be calculated analytically [3] enabling the calculation of accuracy of the implemented SRM algorithm. Synthetic white noise noise was also added to the measurement data. The maximum magnitude of the noise was a percentage of the maximum magnitude of the synthetic near-field data and the phase of the noise was then generated (pseudo) randomly as shown in (3.6).

$$\begin{aligned} |\mathbf{b}_{\text{noise}}| &= \mathbf{rand} * \max(|\mathbf{b}_{\text{analytic}}|) * \frac{\text{noise\_percentage}}{100} \\ \angle\, \mathbf{b}_{\text{noise}} &= \mathbf{randphase} \\ \mathbf{b} &= \mathbf{b}_{\text{analytic}} + \mathbf{b}_{\text{noise}} \end{aligned} \tag{3.6}$$

In (3.6), **rand** is a vector the size of **b** containing pseudo random numbers between 0 and 1. Similarly, **randphase** is a vector the size of **b** containing pseudo random

numbers between $-\pi$ and π. The max(.) function returns the largest element from the vector it operates on. In this case, it is returning the largest magnitude of $\mathbf{b}_{\text{analytic}}$ (the analytically calculated measured data on $\mathcal{S}$). The noise_percentage was the percentage of noise we wanted to use, and $\mathbf{b}$ was synthesized using the analytically calculated values, plus our noise vector.

The frequency of this synthetic test was conducted at 1 GHz, and the CGLS iterations were stopped once the far-field error was below one percent. This was done in order to better show the difference in solving the inverse problem with and without Love's condition. This first small problem was for initial testing of the spherical SRM algorithm, the problem setup is shown in Table 3.1.

Table 3.1: 1 Dipole Problem Setup for Frequency of 1 GHz

Parameter	**Value**
Measurement sphere radius	1.67λ
Reconstruction sphere radius	0.5λ
Number of measurement points	2352
Number of unknowns	1212
Noise added	5%

Note that λ is the wavelength at 1 GHz. The results for this simple problem are shown in Table 3.2. It should be noted that near-field error was calculated as

$$\text{Near-field error} = \frac{\|\mathbf{E}^{NF}_{SRM} - \mathbf{E}^{NF}_{meas}\|_2}{\|\mathbf{E}^{NF}_{meas}\|_2} \times 100\%. \tag{3.7}$$

In (3.7), $\mathbf{E}^{NF}_{SRM}$ is the vector of electric field values calculated from the SRM equivalent current distribution and $\mathbf{E}^{NF}_{meas}$ are the measured field values. Far-field error was calculated in the same way but $\mathbf{E}^{NF}_{SRM}$ and $\mathbf{E}^{NF}_{meas}$ would be replaced with $\mathbf{E}^{FF}_{SRM}$ and $\mathbf{E}^{FF}_{meas}$, respectively. The 'measured' quantities are calculated analytically as mentioned before.

In the case where Love's condition is used, the expected and calculated current distribution on the reconstruction surface $\mathcal{S}'$ was compared according to

$$\text{Error in reconstructed } \mathbf{J} = \frac{\|\mathbf{J}_{SRM} - \mathbf{J}_{True}\|_2}{\|\mathbf{J}_{True}\|_2} \times 100\% \tag{3.8}$$

In (3.8), $\mathbf{J}_{SRM}$ is the reconstructed electric current and $\mathbf{J}_{True}$ is the expected current based on the analytical near-field calculation of the fields on $\mathcal{S}'$ due to the dipole. The error in the magnetic currents are calculated in the same way. It should be noted that this calculation only makes sense for the Love's condition case, because without it, the equivalent currents are not related to the field outside the reconstruction surface and we are not trying to reconstruct the same field of the elementary dipole on $\mathcal{S}'$.

Table 3.2: Simulation Results for 1 Dipole Problem - 1 GHz

Parameter	**Without Love's Condition**	**Love's Condition**
Near-field error	0.68%	0.75%
Far-field error	0.921%	0.889%
Time per CGLS iteration	0.60 s	1.05 s
Number of iterations	7	62
Error in reconstructed $\vec{J}$	N/A	13.29%
Error in reconstructed $\vec{M}$	N/A	16.61%

It can be seen in Table 3.2 that both variations (enforcing Love's condition and not enforcing Love's condition) of the spherical SRM were able to produce far-field errors of less than one percent. As expected, the time per CGLS iteration was much higher when using the Love's condition, as the matrix equation was shown to become larger. It can also be seen that the case where Love's condition was used took many more CGLS iterations to converge to a solution where the far-field error was less than one percent. This is because when using Love's condition, we are setting more conditions that the calculated equivalent currents must meet. These currents must not only be able to produce the desired field on $\mathcal{S}$, but now we also need to produce zero tangential

fields on $\mathcal{S}_{\text{love}}$. In Table 3.2, one can also see that the near-field error was small for both variations of the spherical SRM algorithm. The error in the reconstructed currents are 13.29 % for the electric currents, and 16.61 % for the magnetic currents. The size of these errors can increase or decrease depending on the regularization technique. In this case, we were more interested in the far-field error.

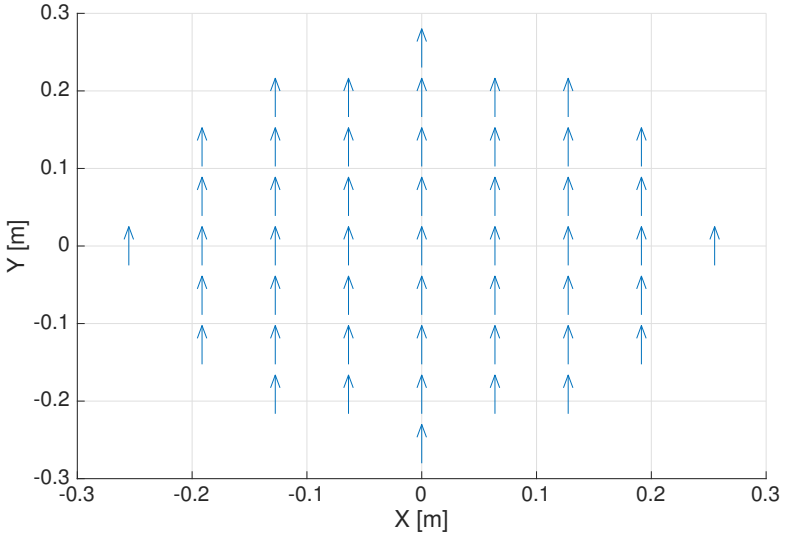

Figure 3.3: Array of y-oriented elementary dipoles used for synthetic testing.

The next test that was conducted was with an array of y-oriented dipoles as shown in Figure 3.3. Love's condition was enforced with this test, and the equivalent currents were reconstructed on a rectangular box enclosing the array of dipoles. An illustration of the reconstruction box mesh is shown in Figure 3.4. The frequency of operation for this test was 1.175 GHz. The rest of the problem setup details are shown in Table 3.3.

Table 3.3: Dipole Array Problem Setup for Frequency of 1.175 GHz

Parameter	**Value**
Measurement sphere radius	5λ
Reconstruction box dimensions (x, y, z)	2.5λ by 2.5λ by 0.2λ
Love's box dimensions (x, y, z)	2.3λ by 2.3λ by 0.1λ
Number of measurement points	14762
Number of unknown edges	3423
Number of Love's points	3520
Noise added	1%

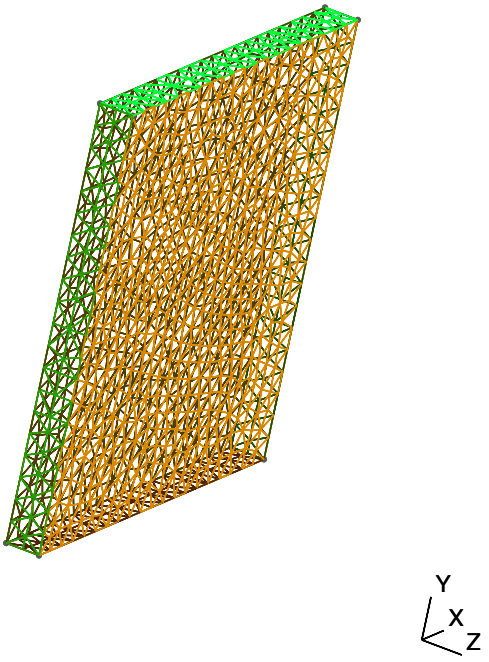

Figure 3.4: The reconstruction surface $\mathcal{S}'$ for the dipole array test.

In Figure 3.5 the magnitude of the far-field patterns calculated analytically from the dipole array, and from the spherical SRM algorithm is shown. The far-field magnitude is shown plotted for an unwrapped sphere.

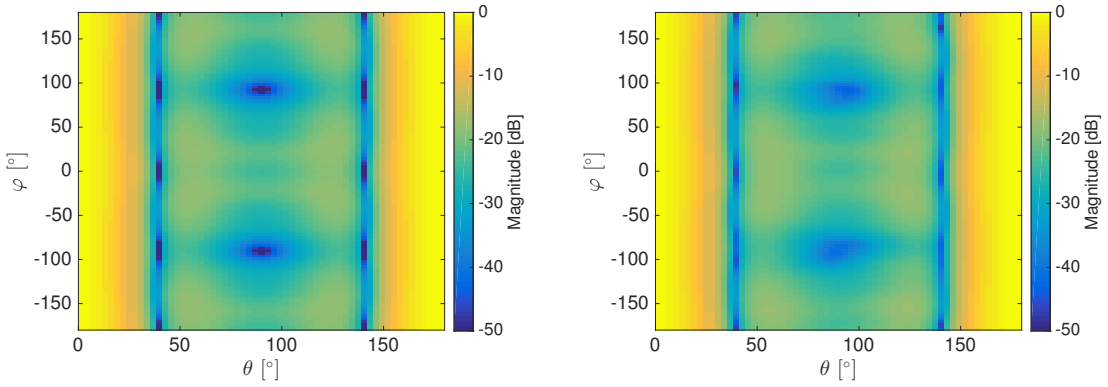

(a) (b)

Figure 3.5: Magnitude of the true [left] and SRM [right] calculated electric far-field patterns over an unwrapped sphere for the dipole array in Figure 3.3 for a frequency of 1.175 GHz.

The far-field magnitude error for this test was 0.75% as calculated in (3.9) where the labels of the variables follow a similar convention to (3.7). In (3.9) the |.| operator map to to the element-wise magnitudes of the vectors they are operating on. In order to show the diagnostic capability of the SRM, we modified the dipole array to remove two of the elements. This new array, is shown in Figure 3.6, and simulates an array that is not functioning properly. Other than the missing elements, the problem is the same as in Table 3.3.

$$\text{Far-field magnitude error} = \frac{\||\mathbf{E}^{FF}_{SRM}| - |\mathbf{E}^{FF}_{\text{analyitic}}|\|_2}{\||\mathbf{E}^{FF}_{\text{analyitic}}|\|_2} \times 100\%. \tag{3.9}$$

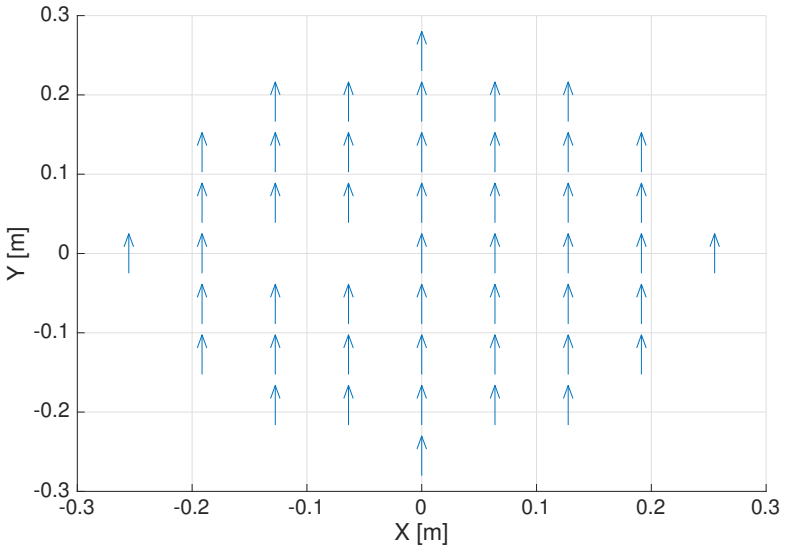

Figure 3.6: New array of y-oriented elementary dipoles used for synthetic testing. Two elements have now been turned off.

Figure 3.7 shows the far-field pattern in the same format as the complete dipole array; the far-field magnitude error in this case was 0.81%. If the far-field patterns of the two dipole arrays are compared, it is difficult to tell what the problem is.

It is also difficult to point out the difference between the two arrays when looking at the magnitude on the near-field measurement surface $\mathcal{S}$ as shown in Figure 3.8.

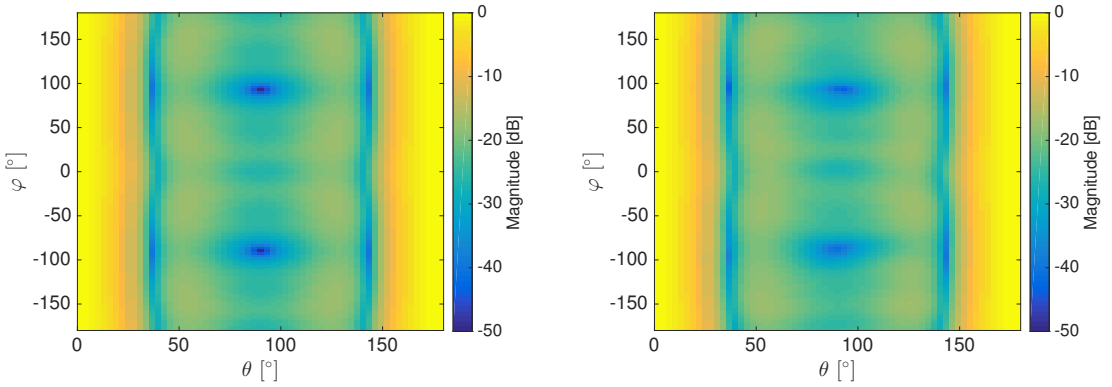

(a) (b)

Figure 3.7: Magnitude of the true [left] and SRM [right] calculated electric far-field patterns over an unwrapped sphere for the dipole array in Figure 3.6 for a frequency of 1.175 GHz.

A clear difference can be seen by looking at the equivalent currents of the different dipole array configurations. In Figure 3.9, the different dipole configurations, electric and magnetic current densities are all plotted for comparison. The equivalent currents show a difference between the two configurations and would also allow an antenna engineer/tester to clue in on the problem/missing elements.

3.2.2 Experimental Tests

In this section we tested our spherical SRM implementation against experimental data from commercially available antennas. The near-field data for these antennas was measured by a commercial system manufactured by Nearfield Systems Inc. (NSI)[2]. This near-field data was extracted by the NSI 2000 software in the Antenna Laboratory at the University of Manitoba. The NSI 2000 software is capable of calculating the far-field pattern from measured near-field data via ME algorithms. In order to compare our SRM implementation with ME, we used near-field data extracted by the NSI 2000 software

[2]Thank you to NovAtel Inc. (Calgary, AB) for providing the raw measured data.

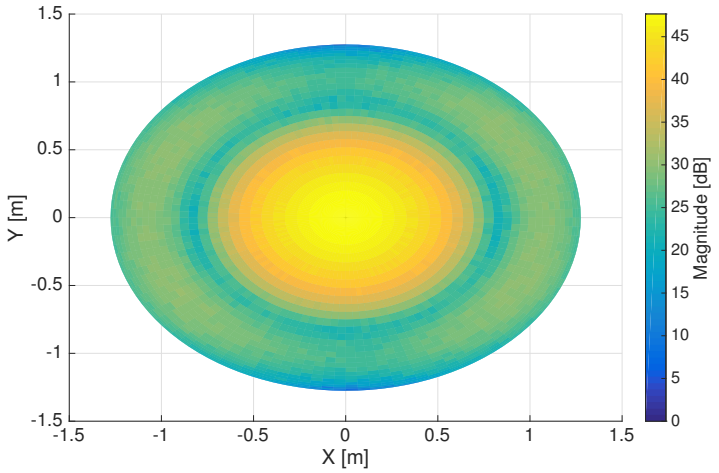

(a)

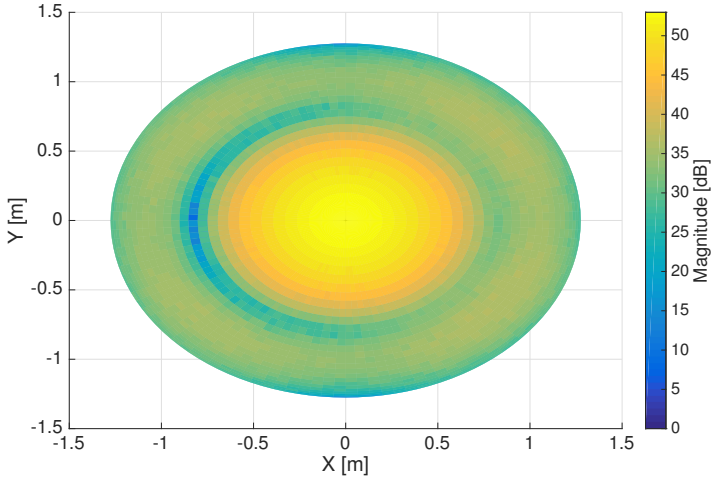

(b)

Figure 3.8: Magnitude of the electric near-field on $\mathcal{S}$ of the full dipole array [top] and the dipole array with missing elements [bottom]. This perspective is looking toward the negative z-axis.

and obtained the far-field with our SRM algorithm and ME. This was done with 100 CGLS iterations. The comparison between ME and SRM is presented below.

It should be stated that we are not calculating the true the far-field pattern through spherical SRM or ME. For these tests, we were not given the true far-field pattern of the AUT, and therefore no judgement about the accuracy of these two methods should be made[3]. Instead we look at the discrepancy between ME and SRM. We calculated the

[3]An accurate far-field pattern for this AUT may be obtained by using a state-of-the-art CATR. Simulations are often not as accurate due to inaccuracies in the assumed model of the AUT *e.g.* material parameters.

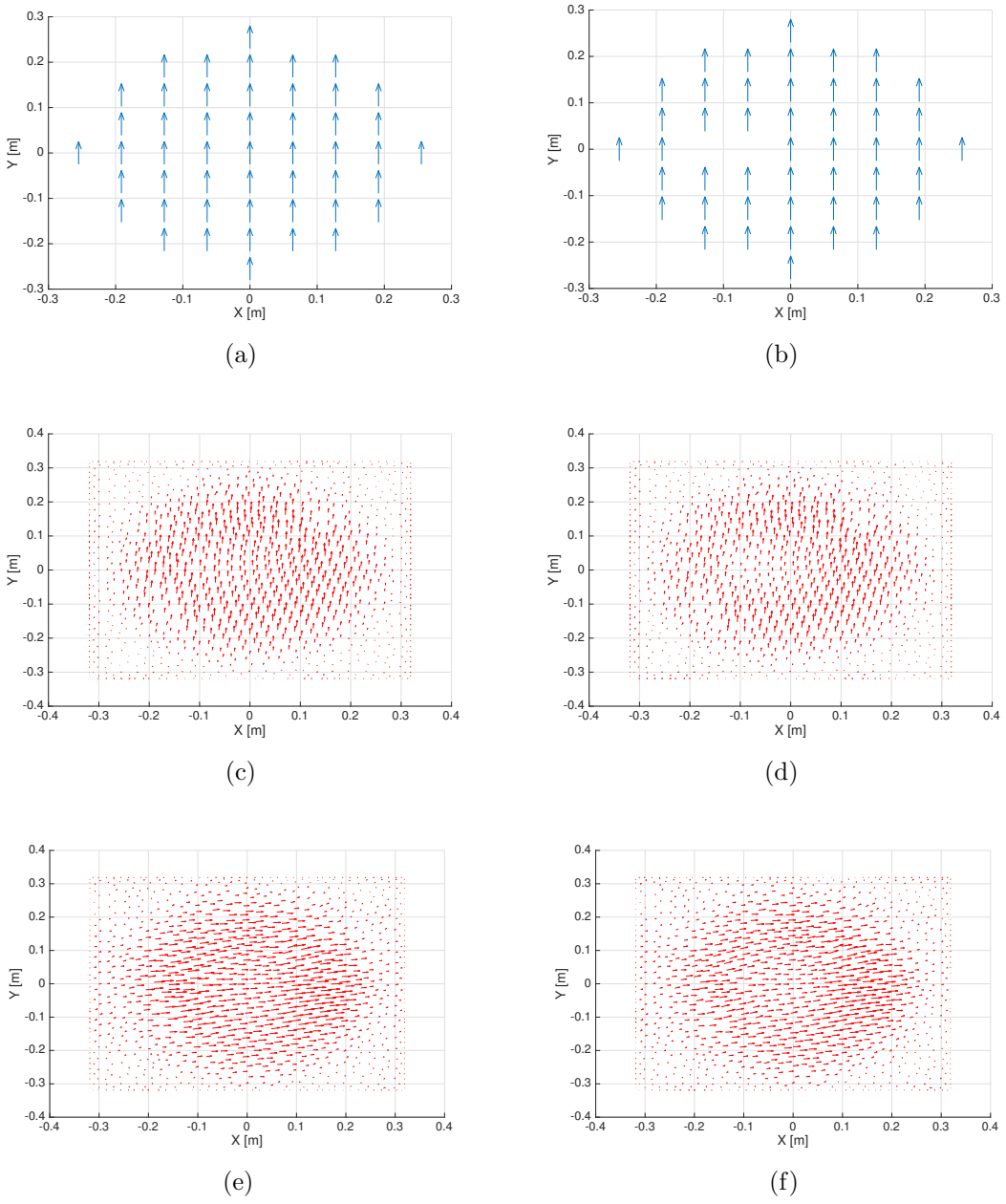

Figure 3.9: Equivalent current density distributions on the reconstruction surface shown for the full dipole array [left column] and array with missing elements [right column]. Both the electric current density [middle row] and magnetic current density [bottom] row are plotted as vectors where the length of the vector represents the relative magnitude of the current. One can see that the currents can show an antenna engineer/tester that one of the arrays is not functioning properly, and also gives a clue to which elements are malfunctioning.

discrepancy as

$$\delta = \frac{\| |\mathbf{E}_{SRM}| - |\mathbf{E}_{ME}| \|_2}{\| |\mathbf{E}_{ME}| \|_2} \times 100\%. \tag{3.10}$$

In (3.10), $\mathbf{E}_{SRM}$ are the electric field values from the SRM and $\mathbf{E}_{ME}$ are the electric field values from ME in vector form. This discrepancy gives us a gauge as to how well our SRM implementation does against the industry standard near-field to far-field transformation technique. It was known that the provided antenna was strongly right-hand circularly polarized (RHCP). Therefore the co-pol, or desired polarization refers to the RHCP component and the cross-pol (x-pol) is not. The co-pol and cross-pol were calculated in our code with reference to [40].

Results are shown at three separate frequencies: 1.175 GHz, 1.275 GHz, and 1.575 GHz. Results for the 1.175 GHz test are shown in full (far-field patterns as well as equivalent current distributions) and results for the other two frequencies are shown in a summarized format due to similarity. The far-field pattern was computed with an angular separation of three degrees resulting in 7381 comparison points. Problem setup information and results are shown in tables below. The different categories of these tables are now explained.

- **Measurement sphere radius:** The radius of $\mathcal{S}$.
- **Reconstruction sphere radius:** The radius of $\mathcal{S}'$. In accordance with the equivalence principle, this radius must be larger than the maximum radial extent (MRE) of the AUT.
- **Number of measurement points:** The number of locations in the near-field where the electric field was sampled.
- **Number of unknowns:** The total number of unknown quantities the inverse solver is calculating. These unknowns directly relate to $\mathbf{x}$.

- **Number of CGLS iterations:** The number of CGLS iterations performed during the test.
- **Pre-processing time:** The time required before CGLS iterations begin. This time is mostly operator matrix ($\mathbf{A}$) build/storage time.
- **Time per CGLS iteration:** The amount of time required to complete CGLS iteration.
- **Time to compute far-field:** The amount of time required for the direct problem where the far-field is calculated from the reconstructed equivalent currents.
- **Co-pol discrepancy (normalized magnitude):** The discrepancy between the co-pol electric field component magnitude in the far-field see (3.10) above.
- **Cross-pol (x-pol) discrepancy (normalized magnitude):** The discrepancy between the x-pol electric field component magnitude in the far-field see (3.10) above.
- **Near-field error:** See (3.7).
- **Memory:** The maximum amount of RAM used.

Co-pol and x-pol magnitude and phase cuts are plotted in the far-field in Figures 3.10-3.12 for both the SRM and ME. These cuts are over the theta coordinate for a fixed phi.

The availability of the equivalent current distribution is one of the main advantages of the SRM. Figures 3.13 and 3.14 show both the tangential components of the electric current density on the reconstruction sphere $\mathcal{S}'$. Figure 3.13 shows these currents viewed from $\theta = 0^\circ$ while Figure 3.14 shows the currents from the opposite vantage point; θ

Table 3.4: Experimental Setup and Results - 1.175 GHz

Parameter	**Value**
Measurement sphere radius	2 m (7.83 λ)
Reconstruction sphere radius	0.28 m (1.10 λ)
Number of measurement points	1891
Number of unknowns	11412
Number of CGLS iterations	100
Pre-processing time	24 min
Time per CGLS iteration	11 s
Time to produce far-field	17 min
Co-pol discrepancy (normalized magnitude)	1.05%
X-pol discrepancy (normalized magnitude)	5.41%
Near-field data misfit	1.97%
Memory Required	2.93 GB

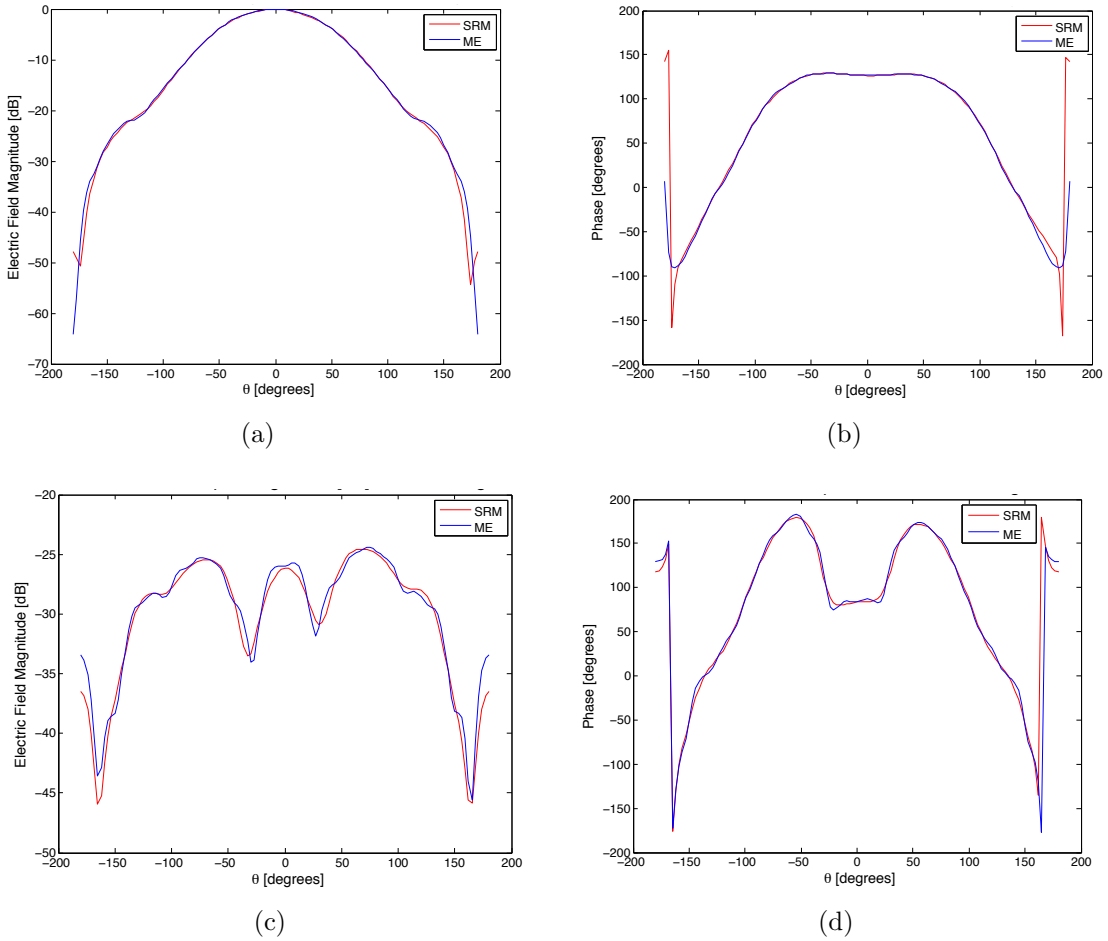

Figure 3.10: Magnitude [left] and phase [right] plots for the $\varphi = 0°$ far-field cut for a frequency of 1.175 GHz. The co-pol [top row] and x-pol [bottom row] patterns are shown.

$= 180°$. These figures were plotted with Paraview[4]. The magnetic current distribution

[4]http://www.paraview.org

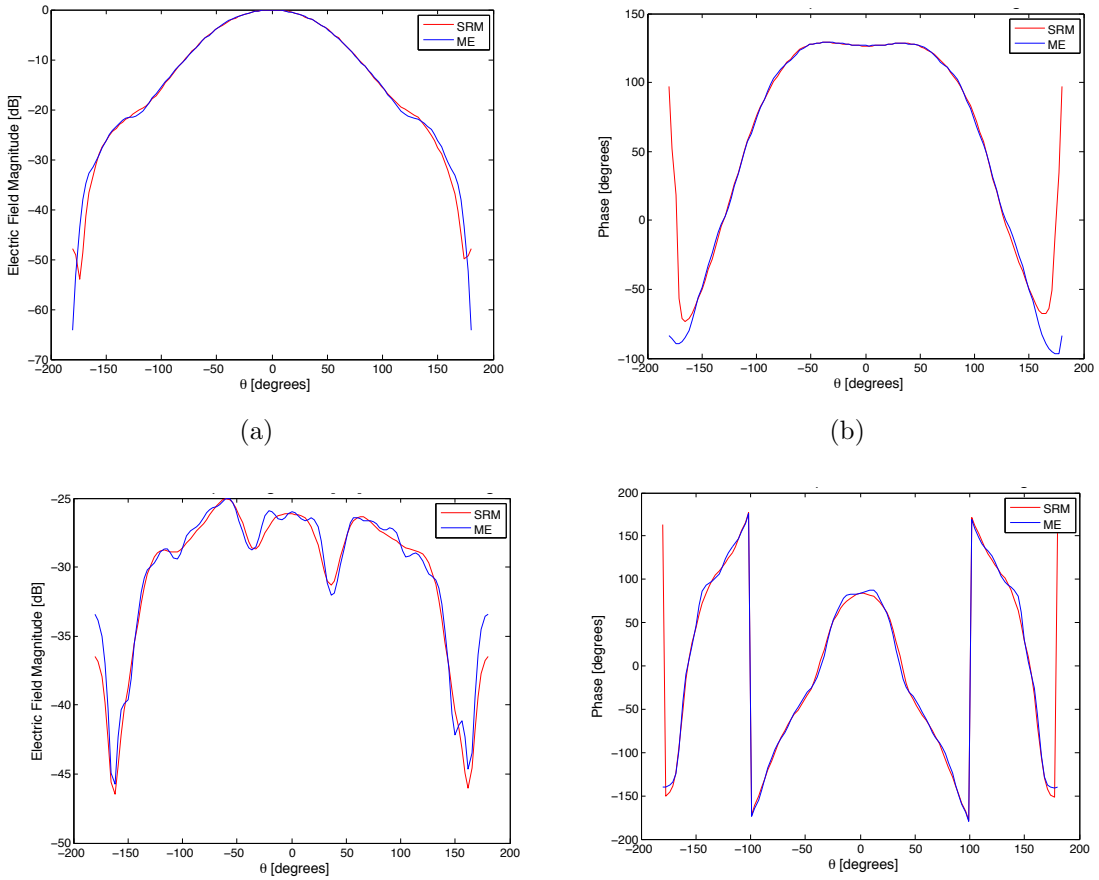

Figure 3.11: Magnitude [left] and phase [right] plots for the φ = -45° far-field cut for a frequency of 1.175 GHz. The co-pol [top row] and x-pol [bottom row] patterns are shown.

was similar to the electric currents, and are not shown here.

Another advantage of the SRM that was mentioned earlier is the ability to forego a complete set of tangential measurement data over the entire closed surface $\mathcal{S}$; *i.e.* we can have an open $\mathcal{S}$. To this end, another test, similar to that outlined in Table 3.4 was performed where this time, measurements over $\mathcal{S}$ were not taken after $\theta > 150$ °. The ME algorithm still used data on a complete spherical surface. The results of this test are summarized in Table 3.5. Figure 3.15 shows the far-field cut when $\varphi = 0°$.

Finally, to test the SRM against the ME over different frequencies, tests were also done at 1.275 GHz and 1.575 GHz. The results of these tests are summarized in Tables 3.6-3.7.

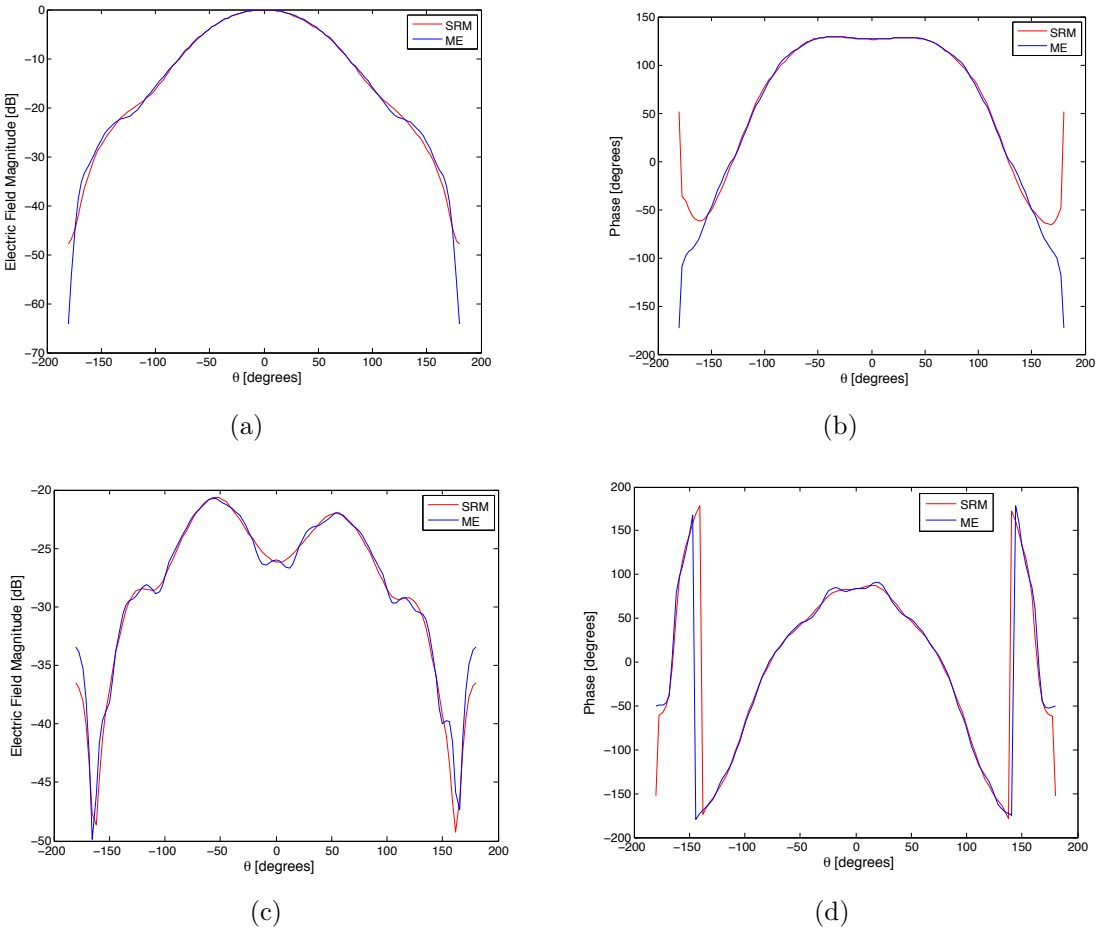

Figure 3.12: Magnitude [left] and phase [right] plots for the φ = -90° far-field cut for a frequency of 1.175 GHz. The co-pol [top row] and x-pol [bottom row] patterns are shown.

Table 3.4 shows that the discrepancy between our implemented SRM algorithm and the NSI 2000 ME algorithm is very small for the 1.175 GHz frequency. We can see that the co-pol discrepancy is close to 1.05 % while the x-pol discrepancy is less 5.41 %. This supports the fact that the SRM is viable method for antenna measurement applications because it has a low discrepancy from a commercially available ME algorithm. Nothing can be said about the accuracy of these two methods unless the far-field pattern of the AUT is measured in a state-of-the-art far-field range. Furthermore, looking at Figures 3.10-3.12, we can see that for both magnitude and phase for all the given cuts and polarizations, the agreement between ME and the spherical SRM algorithm is apparent.

Figures 3.13 and 3.14 show the equivalent electric current distribution produced by the

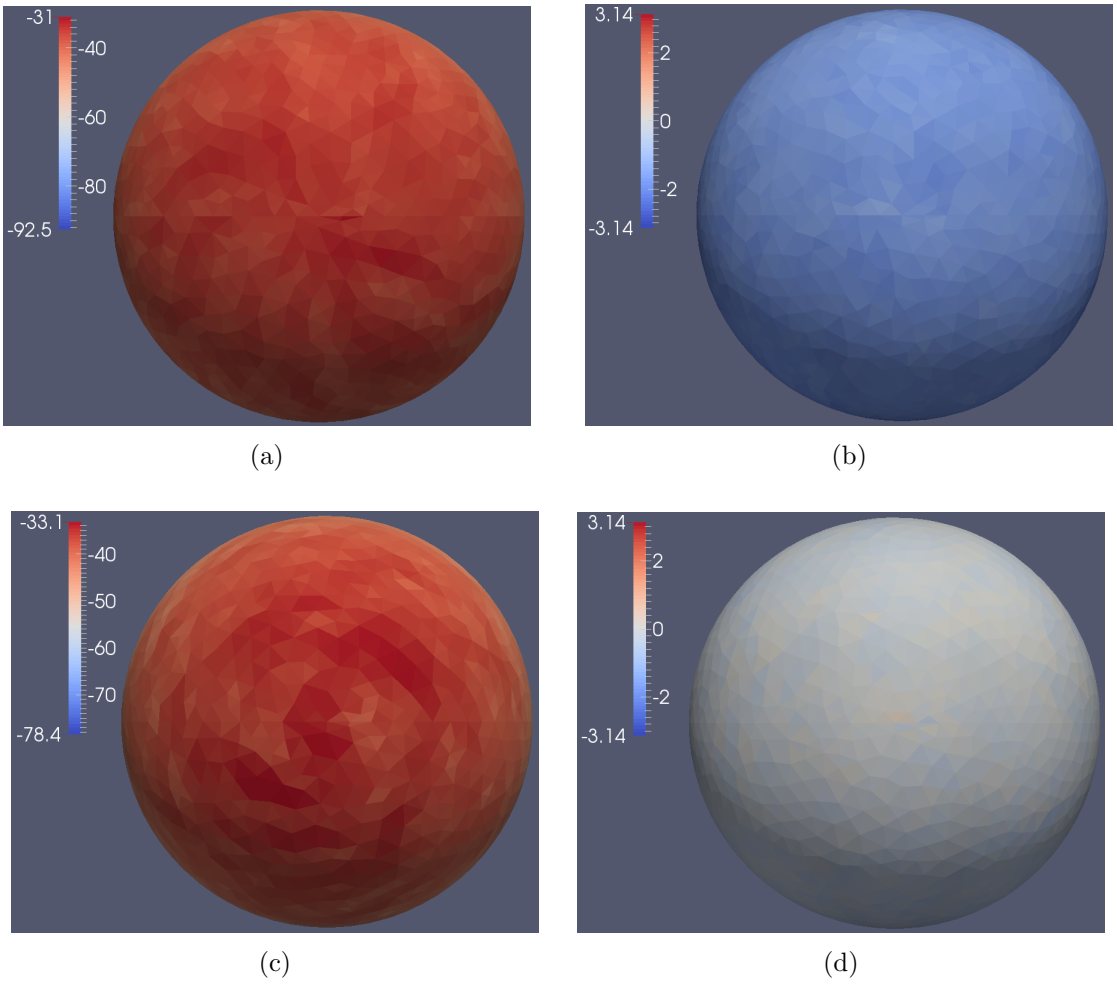

(a) (b)

(c) (d)

Figure 3.13: Equivalent $\vec{J}$ viewed from $\theta = 0°$ for a frequency of 1.175 GHz. The magnitude [dB] [left] and phase [rad] [right] of $\mathbf{J}_\theta$ [top] and $\mathbf{J}_\phi$ [bottom] is shown.

spherical SRM problem for the 1.175 GHz problem. This current distribution conveys a lot of information about the AUT. It was known before-hand that the AUT was strongly circularly polarized. The current distribution reflects this circular polarization of the AUT in Figure 3.13 (b) and Figure 3.13 (d). These figures show that the two polarizations theta and phi are about 90° apart in the θ=0° direction (direction of the main beam). It was also known that this antenna was very directive. It is shown in the magnitude plots of Figures 3.13-3.14 that the antenna is focused even in the near-field because the field strength away from the main beam decreases greatly (at least 30 dB lower). This near-field information can be used by antenna engineers and designers for

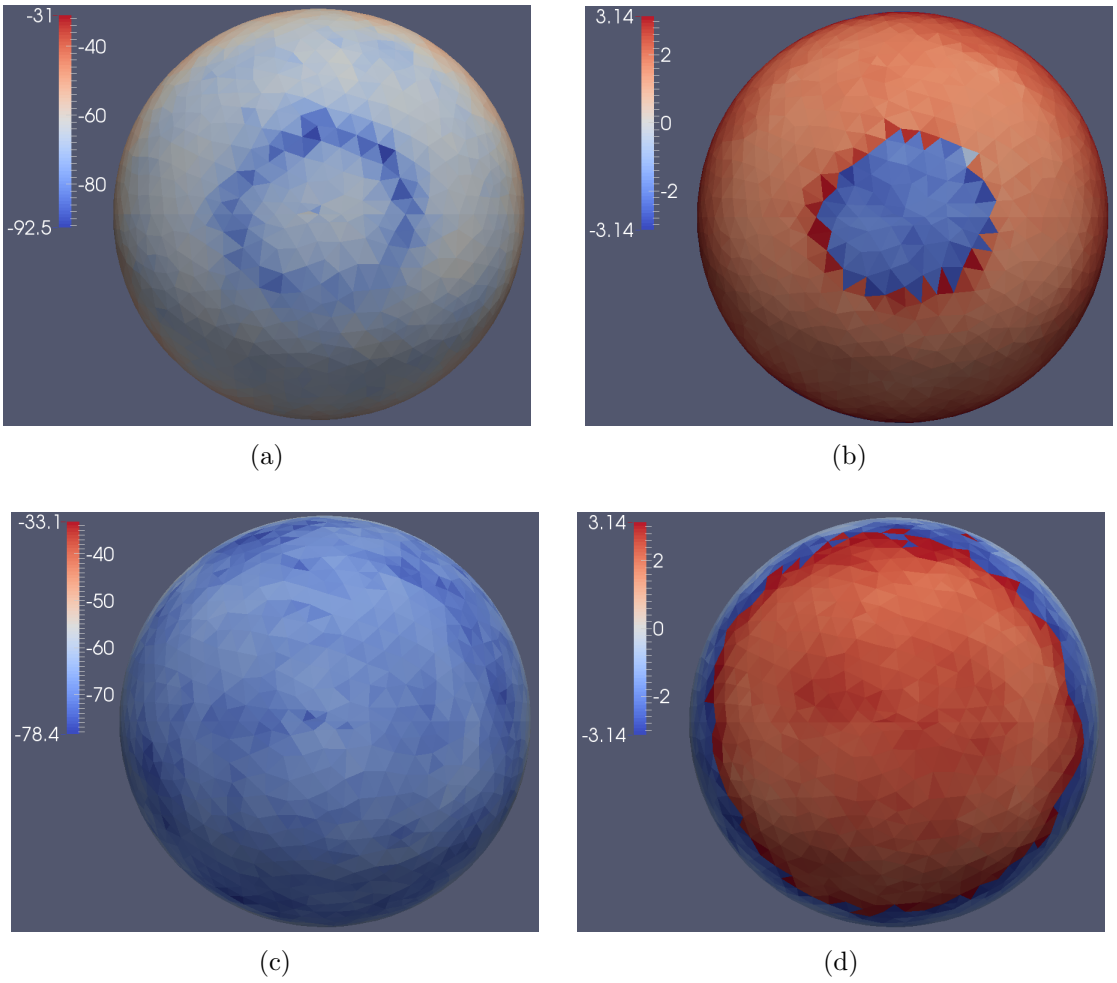

(a) (b)

(c) (d)

Figure 3.14: Equivalent $\vec{J}$ viewed from $\theta = 180°$ for a frequency of 1.175 GHz. The magnitude [dB] [left] and phase [rad] [right] of $\mathbf{J}_\theta$ [top] and $\mathbf{J}_\phi$ [bottom] is shown.

diagnostics purposes.

Table 3.5 summarizes the results from the partial data test where $\mathcal{S}$ was still spherical, but data was not collected if $\theta > 150$ °. The co-pol, x-pol discrepancy, and near-field error are all low and are comparable to the values seen in Table 3.4 where a full measured data set was used as input to our SRM algorithm. It can be seen in Figure 3.15 that even though the ME method made use of the full set of measured values, in this case, the spherical SRM produced a far-field that was comparable. This shows that the SRM algorithm does not need a complete data set over a closed measurement surface. This is important because it is often known (prior information) that a certain region of a set

Table 3.5: Experimental Setup and Results for Partial Data Test - 1.175 GHz

Parameter	**Value**
Measurement sphere radius	2 m (7.83 λ)
Reconstruction sphere radius	0.28 m (1.10 λ)
Number of measurement points	1891
Number of unknowns	11412
Number of CGLS iterations	100
Pre-processing time	23 min
Time per CGLS iteration	11 s
Time to produce far-field	17 min
Co-pol discrepancy (normalized magnitude)	1.06%
X-pol discrepancy (normalized magnitude)	7.53%
Near-field data misfit	1.79%
Memory Required	2.84 GB

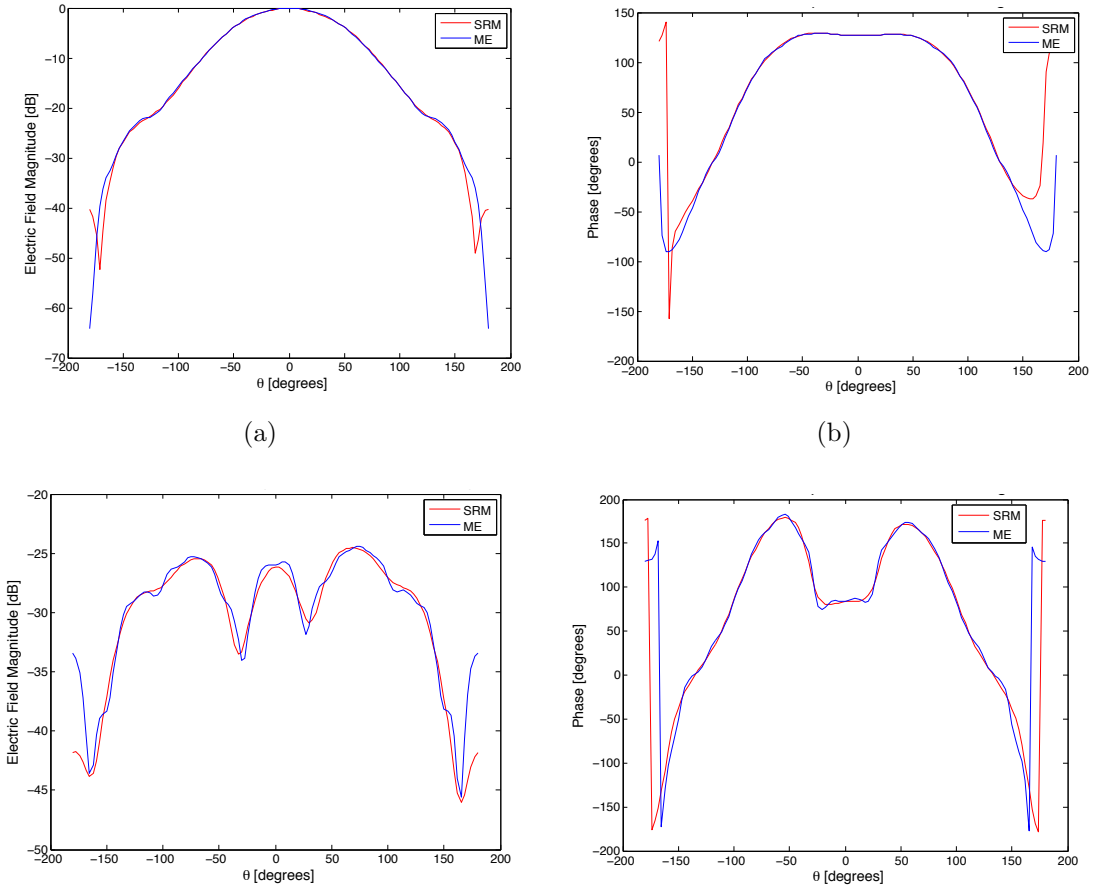

Figure 3.15: Magnitude [left] and phase [right] plots for the $\varphi = 0°$ far-field cut for a frequency of 1.175 GHz. The co-pol [top row] and x-pol [bottom row] patterns are shown.This was a partial data test where no measurements were taken after $\theta > 150$ °for the SRM, but data over the full measurement sphere was given to the ME algorithm.

Table 3.6: Experimental Setup and Results - 1.275 GHz

Parameter	**Value**
Measurement sphere radius	2 m (8.5 λ)
Reconstruction sphere radius	0.28 m (1.19 λ)
Number of measurement points	1891
Number of unknowns	12816
Number of CGLS iterations	100
Pre-processing time	27 min
Time per CGLS iteration	15 s
Time to produce far-field	20 min
Co-pol discrepancy (normalized magnitude)	0.96%
X-pol discrepancy (normalized magnitude)	3.05%
Near-field data misfit	1.93%
Memory Required	3.29 GB

Table 3.7: Experimental Setup and Results - 1.575 GHz

Parameter	**Value**
Measurement sphere radius	2 m (10.5 λ)
Reconstruction sphere radius	0.28 m (1.47 λ)
Number of measurement points	1891
Number of unknowns	20202
Number of CGLS iterations	100
Pre-processing time	58 min
Time per CGLS iteration	39 s
Time to produce far-field	31 min
Co-pol discrepancy (normalized magnitude)	2.24%
X-pol discrepancy (normalized magnitude)	4.98%
Near-field data misfit	2.92%
Memory Required	7.53 GB

of measured values contains more error than other regions. If using the SRM method, these erroneous regions can be omitted from the data set. Furthermore, ME needs a complete set of data over a closed canonical surface. If measured data is not present over some part of the canonical surface, then assumptions have to be made, and this results in truncation error.

We can see by comparing Tables 3.6, 3.12, and 3.7 that the SRM algorithm and ME algorithm stay comparable over a range of frequencies. It should be noted that as we increase the frequency, the problem size starts to increase. We can see that the memory required for the problem increases to 7.53 GB in the 1.575 GHz. As the frequency

increases the time to construct the operator (pre-processing time) increases greatly. This is because we must increase the amount of unknowns to maintain the same resolution of the solution. Note that the increase in operator size leads to greater CGLS iteration times, and far-field calculation times. All these calculations must be done to calculate the far-field in the SRM. This is the main disadvantage of the SRM when compared to the ME method; the added computational complexity. This issue is addressed in the next section.

3.3 Improving the Source Reconstruction Method Algorithm's Efficiency

This section deals with one of the main problems of the SRM which we saw in Section 3.2.2: the relatively large amount memory and time it can take to use the SRM to solve the inverse problem and then obtain a far-field estimate at microwave frequencies. ME methods are faster because they do not solve an inverse problem, instead near-field measurements are directly transformed to the far-field.

To better understand the problem, we can compare Tables 3.4 and 3.7. The frequency increased by a factor of about 1.34 times between these two tables, and we can see that if we want to keep the amount of unknowns constant per unit electrical area, this has the effect of increasing the unknowns by about the square of the frequency increase. This is why we see an increase from 11412 to 20202 unknowns. Since we try to keep the amount of points on Love's surface equal to the amount of unknowns on the reconstruction surface, this would significantly increase the size of the matrix if trying to solve for meaningful equivalent currents. This increase in operator matrix size causes significant memory and solution time increases for practical problems. Although this does not

lead to large problems by today's standards [41], they are large enough that they would benefit from acceleration. Furthermore it is always beneficial to have almost real-time far-field results when working with an antenna measurement system.

In order to address this problem, we chose to investigate the use of the hierarchical matrix (or $\mathcal{H}$-matrix) framework for accelerating the SRM. $\mathcal{H}$-matrices allow the approximation of a class of matrices with logarithmic-linear complexity. Approximations to matrix operations (such as addition, matrix-vector product, matrix-matrix product etc.) can also be implemented with logarithmic linear complexity. In this thesis we do not focus on the theory of the $\mathcal{H}$-matrix framework, instead we focus on the advantages and disadvantages of using it in conjunction with the SRM. For a comprehensive review on $\mathcal{H}$-matrices, we direct the reader to [42]. We expected that the $\mathcal{H}$-matrix framework would work well with the SRM because:

1. The separation of the measurement surface $\mathcal{S}$, and reconstruction surface $\mathcal{S}'$ are often far enough away that this should allow for appreciable compression in the operator matrix $\mathbf{A}$ due to the nature of the Green's function.

2. The actual inversion is done with CGLS, which only involves matrix-vector products and hermitian matrix-vector products. The approximations of these operations are easily implemented in the $\mathcal{H}$-matrix framework.

In this section we briefly describe the $\mathcal{H}$-matrix framework and its application with the SRM. We then show results of our investigation with using the $\mathcal{H}$-matrix in conjunction with the SRM.

3.3.1 Storage of Low-Rank Matrices

The storage and memory efficiency increase enabled be the $\mathcal{H}$-matrix framework can be attributed to the efficient storage of low rank matrices. The basic concept is based on outer-product representations of low-rank matrices. For example, if $\mathbf{A} \in \mathcal{C}_u^{m\times n}$, *i.e.* if $\mathbf{A}$ is a complex matrix of size $m \times n$ and maximum rank u, we can store $\mathbf{A}$ in outer product form as

$$\mathbf{A} = \mathbf{U}\mathbf{V}^H \tag{3.11}$$

where $\mathbf{U}$ is a matrix of size $m \times u$ and $\mathbf{V}$ is a matrix of size $n \times u$ [42]. If we store $\mathbf{A}$ in this way, there are $u(m+n)$ entries instead of mn as we would in the full entry-wise representation.

We can see that storing a matrix as in (3.11) facilitates matrix-vector products. Now instead of the original problem $\mathbf{A}\mathbf{x} = \mathbf{b}$ we can instead do

$$\mathbf{U}(\mathbf{V}^H\mathbf{x}) = \mathbf{b} \tag{3.12}$$

where the vector $\mathbf{x}$ and $\mathbf{V}^H$ are multiplied first. Then, bundling multiply and add into one operation for illustrative purposes, the traditional matrix-vector product would take roughly mn multiply-adds while in (3.12) we would have about $u(m+n)$ multiply-adds. It is easy to see that if

$$u(m+n) < mn \tag{3.13}$$

we will need less memory to store **A** and faster matrix-vector product time associated with **A** and we can call **A** a low rank matrix. Note that due to the requirements of the CGLS algorithm, we are only concerned with matrix-vector products for our implementation therefore none of the other $\mathcal{H}$-matrix factorizations and operation approximations are explored in this thesis [42].

3.3.2 Low-Rank Matrix Approximation

The forward operator matrices required for our SRM implementations are usually full rank in nature, but (at least) partitions of these operator matrices can be approximated as low rank matrices due to the nature of the Green's function. This is essential to the $\mathcal{H}$-matrix framework, in which sub-blocks of the overall matrix are hierarchically approximated as low rank matrices based on a user-defined condition. One error controllable way to approximate a matrix of arbitrary rank by an outer-product matrix with rank u is to use a truncated SVD [42]. However, a problem with this method is that you need to build the entire sub-matrix to perform the SVD and this takes time. To save build time, we have utilized the adaptive cross approximation (ACA) to build sub-matrices (in outer product form) that have been chosen for compression. With this approach, we never have to build the entire sub-matrix, just enough rows and columns that are able to meet the error criterion at user selected test points *i.e.* the 'true' operator values are only needed for the entries corresponding to the test points which are small in quantity (around 1% in our case) compared to the total amount of elements. For details on our implementation we direct the reader to [43].

3.3.3 Choosing Sub-Blocks to Approximate as Low Rank

It is usually not possible to approximate the entire matrix such that the error in that approximation is low, and the matrix meets the condition in (3.13). In the $\mathcal{H}$-matrix framework, sub-blocks of the full matrix are hierarchically chosen for compression based on a user defined condition. The condition that was used in our implementation was

$$\nu > \frac{\max(\text{diam}(X_m), \text{diam}(X_s))}{\text{dist}(X_m, X_s)} \tag{3.14}$$

where ν is the user selected admissibility parameter, X_m refers to the group of measurement points corresponding to the sub-matrix for which we are calculating this condition, and X_s refers to the group of source points corresponding to the same sub-matrix.

In (3.14), we are comparing the maximum (max(.)) diameter (diam(.)) of the two groups of points to the distance (dist(.)) between the two groups of points. The condition itself may best be explained through an analogy. Consider the light from two stars in the night sky. This light radiates according to an appropriate Green's function to the receivers at the measurement locations which are your eyes. If those two stars (X_s) are far enough away from your eyes (X_m), then they start to look like one star. In this case the denominator in (3.14) would become large, and the overall fraction would become small. Similarly, if the distance between the two stars starts to decrease, they start to look like one star at the measurement locations (*i.e.* the maximum diameter is decreasing). In this case the numerator of (3.14) is getting smaller, and the overall fraction is still getting smaller. This example shows that as (3.14) gets smaller, we may be able to approximate X_s as a simpler source and consequently, the corresponding sub-matrix as

low rank. The condition in (3.14) is referred to as an admissibility condition, and the reader can find a more in depth discussion on admissibility conditions in [42].

It should be mentioned that we assume that the full operator matrix is ordered in such a way that the sub-blocks of the full operator contain groups of source points and measurement points that are in geometric proximity *i.e.* the source points are in general proximity to each other and the measurement points are in general proximity (the separate groups X_s and X_m are not guaranteed to be in proximity), this is discussed further in Section 3.3.4. It is also important to mention that admissibility conditions do not usually lead to an optimal $\mathcal{H}$-matrix compression, but do, in general, provide enough to compression to obtain considerable performance gains [42]. Finally, since measurement points and source points are usually placed at regularly spaced intervals, a larger admissibility parameter ν usually leads to larger sub-matrices being compressed. Furthermore, sometimes even the smallest sub-blocks do not meet the admissibility condition. If this is the case, they are stored as dense matrices and are not compressed.

3.3.4 Building the $\mathcal{H}$-matrix

In order to exploit the low-rank matrix representations to compress the discrete forward operator $\mathbf{A}$ it is necessary to order the matrix in such a way that sub-blocks are compressible. This was facilitated by first reordering the matrix according to geometrical clustering [42] of the measurement and source points. This ensures that each sub-block we test with our admissibility condition correspond to measurement points and source points with geometric locality. Otherwise we may never meet the admissibility condition for any sub-block *e.g.* if there is no geometric locality then there is no guarantee that smaller and smaller sub-blocks correspond to clusters that have smaller diameters or that the distance between X_s and X_m changes. The two cluster trees (that resulted from our

geometrical clustering) T_m and T_s corresponding to the measurement and source points, respectively, and were used to create the $\mathcal{H}$-matrix structure. For an in depth discussion on how this is done, we refer the reader to [42].

3.3.5 Results from using the $\mathcal{H}$-matrix Framework with the Source Reconstruction Method

The results of our investigation of using the $\mathcal{H}$-matrix framework with the SRM are shown. First we show results with the SRM without using Love's condition, then with Love's condition.

3.3.5.1 $\mathcal{H}$-matrix Acceleration of the Source Reconstruction Method without Love's Condition

First, a synthetic problem was created in which Love's condition was not enforced. This might be the case if the user of the SRM only wants a far-field pattern. The problem characteristics are shown in Table 3.8. The sampling was done as in [44] to ensure realistic problem sizes.

Table 3.8: $\mathcal{H}$-matrix test with SRM and no Love's Condition

Parameter	**Value**
Measurement sphere radius	5 λ
Reconstruction sphere radius	1 λ
Number of measurement points	7381
Number of unknowns	3051
Total Operator Matrix Size	14762 by 6102
Frequency	1.175 GHz
CGLS iterations	200

The source that was used for this test was a simple array of five dipole infinitesimal dipole antennas oriented in the y-direction as shown in Figure 3.16.

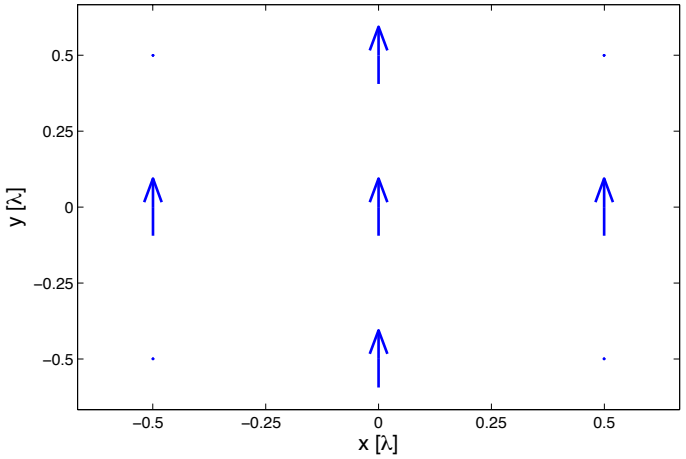

Figure 3.16: Array of y-oriented 5 infinitesimal dipoles used as the source for our $\mathcal{H}$-matrix with SRM synthetic tests. This figure is courtesy of Trevor Brown.

The properties used to generate the $\mathcal{H}$-matrix for this test are shown in Table 3.9.

Table 3.9: $\mathcal{H}$-matrix Properties for no Love's Condition Test

Parameter	**Value**
Maximum points in leaves of $\mathcal{S}$ Cluster Tree: T_m	150
Maximum points in leaves of $\mathcal{S}'$ Cluster Tree: T_s	150
Error in admissible blocks	1 %
Percentage of test points used with ACA	1%

For this test we held the parameters in Table 3.9 constant while varying the admissibility parameter for the $\mathcal{H}$-matrix. We solved the inverse problem that is associated with the SRM with the resulting $\mathcal{H}$-matrices and monitored three important properties that characterize the efficiency of the solution: build speedup, CGLS speedup, and memory compression.

Build speedup is a comparison between the time taken to build the full operator matrix with and without using the $\mathcal{H}$-matrix framework. If $\text{Time}_{\text{full}}$ is the time it took to fill the full operator matrix $\mathbf{A}$, and $\text{Time}_{\mathcal{H}}$ is the time it took to build the $\mathcal{H}$-matrix approximation of $\mathbf{A}$, we can summarize build speedup as

$$\text{Build Speedup} = \frac{\text{Time}_{\text{full}}}{\text{Time}_{\mathcal{H}}}. \tag{3.15}$$

Therefore, according to (3.15), the greater the build speedup, the less time it took to build the $\mathcal{H}$-matrix approximation than compared to the full operator $\mathbf{A}$.

CGLS speedup is similar to (3.15), but is based on the time it takes to complete 200 iterations of CGLS with the full operator matrix $\mathbf{A}$ compared with the time needed to complete the 200 iterations using the $\mathcal{H}$-matrix approximation of $\mathbf{A}$. If $\text{Time}_{\text{fullCGLS}}$ is the time taken to complete 200 iterations of CGLS with the complete $\mathbf{A}$, and $\text{Time}_{\mathcal{H}\text{CGLS}}$ is the time taken to complete the same number of iterations using the $\mathcal{H}$-matrix framework, then we can describe CGLS speedup as

$$\text{CGLS Speedup} = \frac{\text{Time}_{\text{fullCGLS}}}{\text{Time}_{\mathcal{H}\text{CGLS}}}. \tag{3.16}$$

Since CGLS only involves matrix vector products with the operator matrix, (3.16) directly relates to the matrix-vector product speedup.

Finally, memory compression is the comparison of memory taken to represent the full matrix Mem_{full} to the memory taken to represent the $\mathcal{H}$-matrix approximation $\text{Mem}_{\mathcal{H}}$ as shown (3.17).

$$\text{Memory Compression} = \frac{\text{Mem}_{\text{full}}}{\text{Mem}_{\mathcal{H}}}. \tag{3.17}$$

The results obtained from monitoring these values as the admissibility was changed are shown in Figure 3.17.

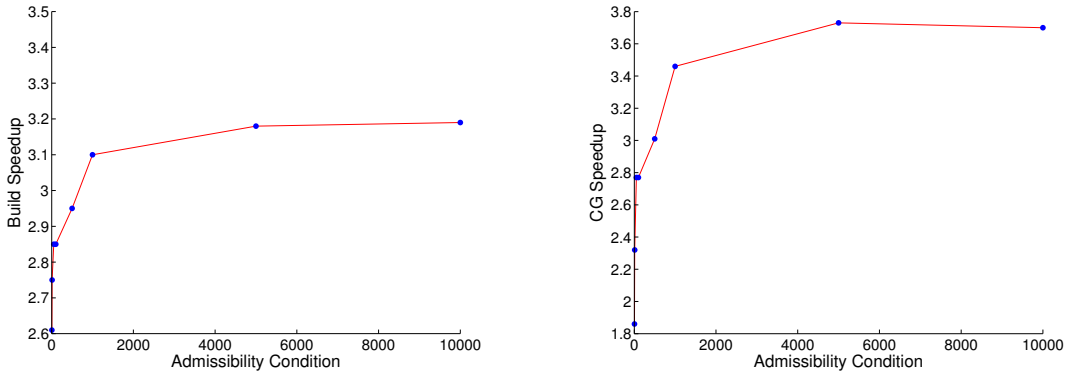

(a)

(b)

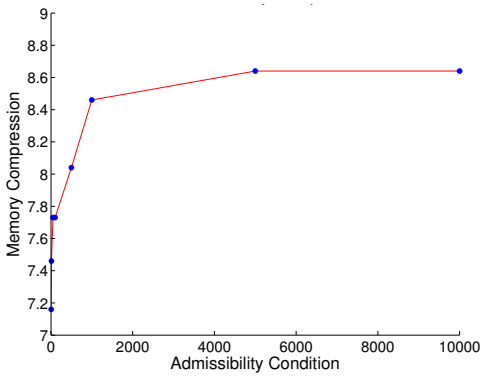

(c)

Figure 3.17: The build speedup (a), CG speedup (b), and memory compression (c) for varying admissibility condition parameter values. This case was done without Love's condition.

In Figure 3.17, as the admissibility tolerance increases, at first the build speedup increases rapidly then slowly levels off. The same pattern is observed for both the CG speedup and the memory compression. Recall that increasing the admissibility tolerance leads to larger sub-blocks being compressed. Consequently, as we compress larger blocks we are seeing more benefit in terms of speedup and memory compression.

In order to test the extreme case, we compressed the full parts of the operator matrix $\mathbf{A}$ that correspond to the different currents (electric and magnetic) and polarizations ($\hat{\theta}$ and $\hat{\varphi}$) as in (3.3). This produced the best results in terms of build speedup, CG speedup, and memory compression.

- Build speedup = 4.48

- CG speedup = 10.7
- Memory compression = 12.0

These results indicate that it is *not* beneficial to use the $\mathcal{H}$-matrix framework with the SRM without Love's condition. Instead, one should just compress as much of the operator matrix as possible (*e.g.* using the ACA).

3.3.5.2 $\mathcal{H}$-matrix Acceleration of the Source Reconstruction Method with Love's Condition

Note that when building the $\mathcal{H}$-matrix structure $\mathbf{A}_{\mathbf{j}\theta}$, $\mathbf{A}_{\mathbf{m}\theta}$, $\mathbf{A}_{\mathbf{j}\varphi}$, and $\mathbf{A}_{\mathbf{m}\varphi}$ are constructed separately because they are calculated slightly differently, but since they all relate to the same measurement and source points, we only need one $\mathcal{H}$-matrix structure. This also means that we need a separate structure if using Love's condition because the source points (T_s) will stay the same, but now we need to use Love's points on $\mathcal{S}_{\mathbf{love}}$ which require a new geometric cluster tree (say T_l). We could have made one $\mathcal{H}$-matrix structure including Love's points as measurement points, but if two separate structures are used, we can easily use two separate admissibility parameters which is advantageous as will be shown later.

A test similar to that of Section 3.3.5.1 was performed but this time Love's condition was enforced. Table 3.10 shows the problem characteristics for the SRM problem with Love's condition. As can be seen, there is now an increase in matrix size due to the addition of Love's points.

Table 3.10: $\mathcal{H}$-matrix test with SRM using Love's Condition

Parameter	**Value**
Measurement sphere radius	5 λ
Reconstruction sphere radius	1 λ
Love's sphere radius	0.9 λ
Number of measurement points	7381
Number of unknowns	3051
Number of Love's points	3016
Total Operator Matrix Size	20794 by 6102
Frequency	1.175 GHz
CGLS iterations	200

The same array of 5 infinitesimal dipoles was used as a source in this test (Figure 3.16). The properties that were used to construct the $\mathcal{H}$-matrix are the same as Table 3.9 with the exception that

- The entire part of the operator **A** that does not deal with enforcing Love's condition (See (3.4)), is compressed completely *i.e.* the admissibility parameter for this part of the operator was set to infinity.

This way, we can see how changing the admissibility parameter affects the efficiency of approximating the Love's part of **A** as we already know that it is best to compress all of the part of **A** that does not deal with Love's condition.

We show the results of these tests in Figure 3.18.

In Figure 3.18 it is shown that the build speedup does not keep increasing for increasing admissibility parameter values. Instead, it increases rapidly, and then starts to decrease again. The admissibility parameter value that this occurs in our plot is 55. This shows that in the case of using Love's condition, the admissibility parameter (size of the admissible blocks) are important, and so using the $\mathcal{H}$-matrix framework is useful as this gives us the choice in picking our admissibility parameter.

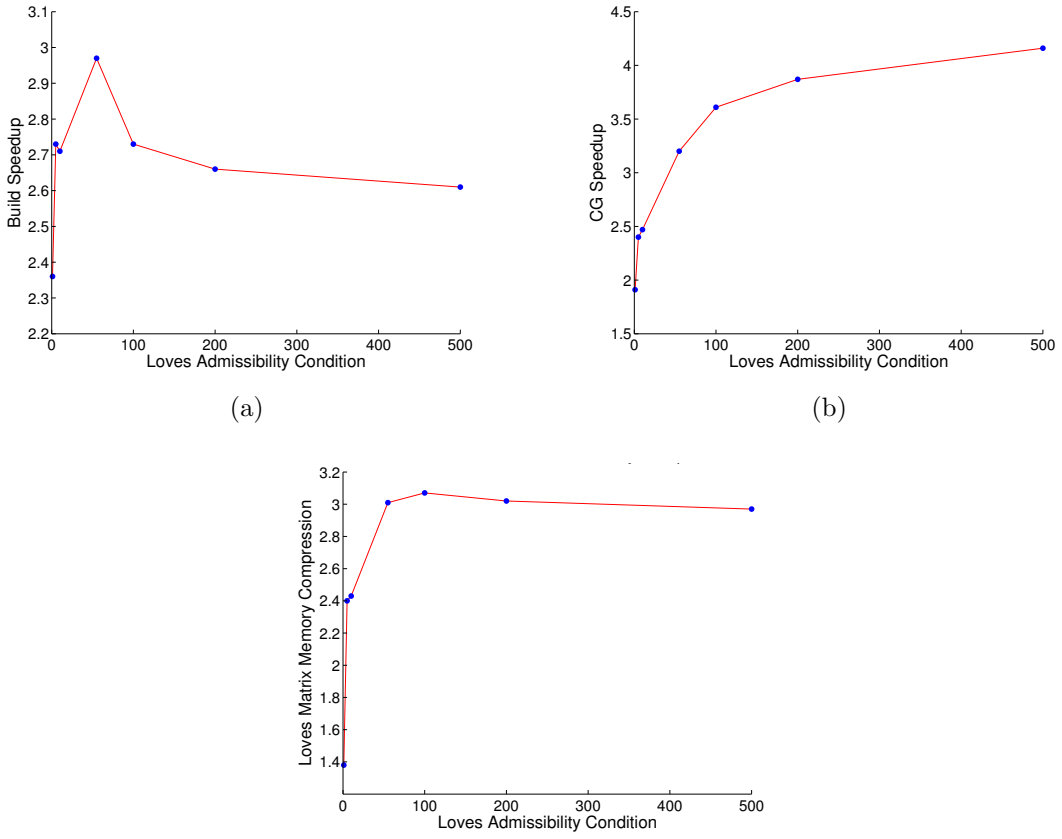

Figure 3.18: The build speedup (a), CG speedup (b), and memory compression (c) for varying the admissibility condition parameter values. This case was done with Love's condition.

The reason the build speedup decreases after a certain admissibility parameter value is because as the admissible matrices become larger and larger, more rows and columns are needed to represent the admissible block for the chosen accuracy level *i.e.* more time is needed to build the extra elements in the larger admissible matrices. This can be seen in Figure 3.19 and 3.20, where we can see that the blocks are all larger when the admissibility is 500 compared to when the admissibility is 55. We can also see that the larger blocks are all warmer colours, which indicates that the need more rows and columns to be approximated, and hence more time to build.

It is also seen in Figure 3.18, that the CG speedup keeps on increasing. This is different than the build speedup which started to decrease after a certain amount of time. This

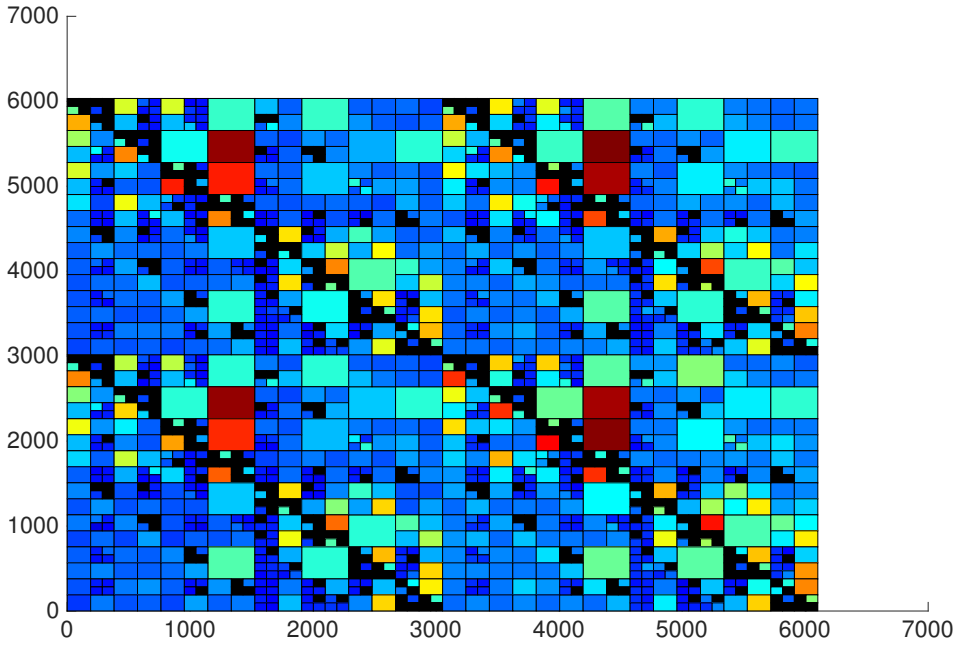

Figure 3.19: The $\mathcal{H}$-matrix structure for Love's part of the operator for an admissibility parameter of 55 (best observed build speedup from our tests). The black squares were stored as dense matrices. Other than the black squares, the warmer colours represent blocks that have a high rank compared to u_{max} and the colder colours are those that have a low rank compared to u_{max}. The parameter u_{max} refers to the largest rank of a compressed matrix.

may be due to the fact that although many more elements must be computed in the build case due to the larger admissible blocks, there are still few enough independent rows and columns in those blocks so that we see speedup in our matrix-vector product time. This can occur if it takes longer to compute individual matrix elements than perform a matrix-vector product. This hypothesis is supported by the memory compression graph because after the admissibility is 55, the memory compression starts to *slowly* drop off, which means that a large amount of memory is not required to store the extra rows and columns that are needed in the sub-matrix approximations.

These results show that it is indeed useful to use the $\mathcal{H}$-matrix framework to approximate the discrete operator matrix $\mathbf{A}$ when Love's condition is being enforced. In general, when there are measurement points both far away (in terms of wavelengths) and near to the

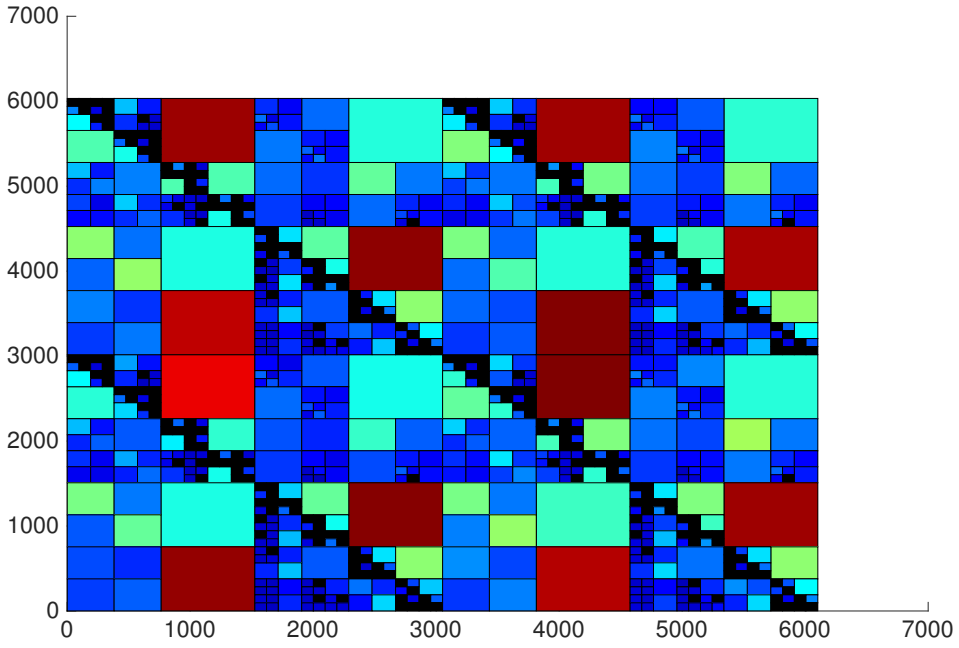

Figure 3.20: The $\mathcal{H}$-matrix structure for Love's part of the operator for an admissibility parameter of 500. The black squares were stored as dense matrices. Other than the black squares, the warmer colours represent blocks that have a high rank compared to u_{max} and the colder colours are those that have a low rank compared to u_{max}. The parameter u_{max} refers to the largest rank of a compressed matrix.

reconstruction surface, the $\mathcal{H}$-matrix framework will be beneficial in SRM. As was shown in the previous section, if all the measurement locations are distant (near-field region) to $\mathcal{S}'$, then it is better to simply compress the full operator.

The SRM has been accelerated before by other techniques. Perhaps the most famous is the multilevel-fast multipole method/algorithm (MLFMM/MLFMA) [25, 26, 45, 46]. We have begun research on comparing the use of MLFMM and the $\mathcal{H}$-matrix framework to accelerate the SRM. This research can be found in Appendix A.

Based on the research conducted here and the preliminary research in Appendix A, the use of the $\mathcal{H}$-matrix framework seems promising for use with the SRM for the frequencies and problem sizes studied, especially for diagnostic applications in which Loves's condition must be enforced.

Chapter 4

Source Reconstruction Method for Microwave Imaging

The SRM is a flexible algorithm and can be used to characterize antennas in many different configurations. In this chapter, we outline our novel method of how the SRM can be used within the context of microwave imaging (MWI). More specifically we will be working with 2D MWI or microwave tomography (MWT). First, we briefly explain what MWT is, and in what way the SRM can be used. Then we explain the SRM algorithm that was developed for use in MWT. Finally, we show synthetic and experimental examples. The work described in this chapter was originally accepted for publishing in [47]

4.1 Source Reconstruction Method Applied to Microwave Tomography

In this section we briefly explain what MWT is and where SRM may be applied in order to see some benefit.

4.1.1 Microwave Tomography

MWT is a modality in which the dielectric profile of an object of interest (OI) in the imaging domain $\mathcal{D}$ can be quantitatively characterized via successive interrogation by a set of transmitters outside $\mathcal{D}$. During the successive interrogation, the total electric field ($\vec{E}_{tot}$) is collected on the measurement domain $\mathcal{S}$ outside of $\mathcal{D}$. The OI is then removed, and the experiment is then repeated to collect the incident field ($\vec{E}_{inc}$) at the receiver positions. The difference between the total field and incident fields are taken to calculate the scattered field ($\vec{E}_{scat}$). The scattered field on $\mathcal{S}$ is then given as input into an inverse scattering algorithm in order to calculate the dielectric profile of the OI [30]. Figure 4.1 shows a popular MWT configuration.

All the measurements in MWT are taken outside of the imaging domain $\mathcal{D}$ that contains the OI, therefore MWT is non-destructive. Furthermore, the OI is interrogated by electromagnetic radiation at microwave frequencies, and therefore MWT is non-ionizing. This non-destructive, non-ionizing nature of MWT makes it a desirable topic of study for use in application areas such as biomedical imaging and non-destructive testing.

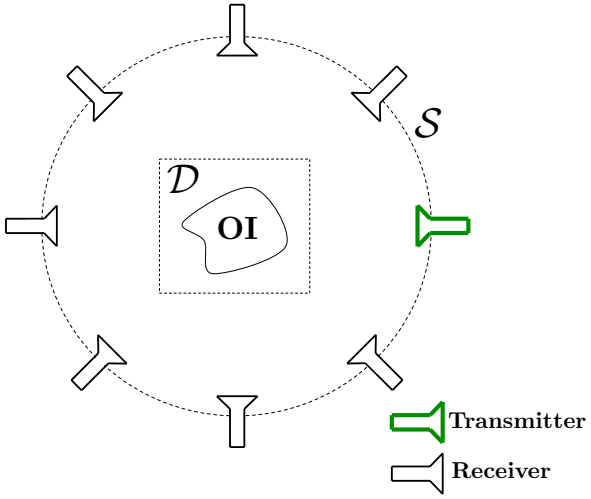

Figure 4.1: A popular MWT configuration where $\mathcal{D}$ is the imaging domain and $\mathcal{S}$ is the measurement domain. This apparatus is in the x-y plane. © [2016] IEEE

4.1.2 Microwave Tomography Inverse Scattering Algorithms

In this section, we will briefly look at how inverse scattering algorithms work to calculate the dielectric profile of the OI. If the reader wants a detailed review of inverse scattering algorithms we suggest [30, 48]. Here we will go over enough in order to see where SRM can be beneficial to inverse scattering algorithms.

Inverse scattering algorithms work by manipulating the well known data and domain equations shown below:

$$\begin{aligned} \vec{E}_{tot}(\vec{r}) &= \vec{E}_{inc}(\vec{r}) + \omega^2 \int_{\mathcal{D}} g(\vec{r},\vec{r}\,')\delta_m(\vec{r}\,')\vec{E}_{tot}(\vec{r}\,')d\vec{r}\,' \\ \vec{E}_{tot}(\vec{r}\,') &= \vec{E}_{inc}(\vec{r}\,') + \omega^2 \int_{\mathcal{D}} g(\vec{r}\,',\vec{r}\,'')\delta_m(\vec{r}\,'')\vec{E}_{tot}(\vec{r}\,'')d\vec{r}\,'' \end{aligned} \tag{4.1}$$

In (4.1) $\vec{r} \in \mathcal{S}$, $\vec{r}\,' \in \mathcal{D}$, $\vec{r}\,'' \in \mathcal{D}$, ω is the angular frequency, and $g(\vec{r},\vec{r}\,')$ is the Green's function, which for a 2D framework is defined as

$$\frac{1}{4j}H_0^2(k_b|\vec{r}-\vec{r}\,'|). \tag{4.2}$$

In (4.2), k_b is the wave number of the background medium, $j^2 = -1$, and $H_0^2(.)$ is the Hankel function of the second kind. The data equation relates the electric field on the measurement surface to the electric field and material properties in the imaging domain, while the domain equation describes a transformation only within the imaging domain. The unknown of interest is the contrast $\delta_m(\vec{r}\,') \in \mathcal{D}$.

$$\delta_m(\vec{r}\,') = \frac{1}{c^2(\vec{r}\,')} - \frac{1}{c_b^2(\vec{r}\,')} \tag{4.3}$$

In (4.3), we see that the contrast $\delta_m(\vec{r}\,')$ can tell us the difference in speeds of the electromagnetic radiation of the background ($c_b(\vec{r}\,')$) and $\mathcal{D}$ ($c(\vec{r}\,')$). Since we should know the speed of the background, and the speed of electromagnetic radiation is defined in terms of the dielectric profile of the (non-magnetic) medium, we can calculate the dielectric profile of the OI.

The problem is that in (4.1) the electric field in $\mathcal{D}$ (not just the contrast) is also unknown, therefore we need both the data (top equation in (4.1)) and domain (bottom equation in (4.1)) to deal with our two unknowns. Different inverse scattering algorithms obtain the dielectric profile by manipulating the equations in (4.1) in different ways. The current state of the art inverse scattering algorithms are multiplicatively regularized Gauss-Newton Inversion (MR-GNI) [49, 50] and multiplicatively regularized contrast source inversion (MR-CSI) [51, 52].

It can be seen from (4.1) that inverse scattering algorithms need the scattered field on $\mathcal{S}$, but also the incident field in $\mathcal{D}$. The incident field $\vec{E}_{inc}$ can be measured on $\mathcal{S}$ in

order to obtain the scattered field on $\mathcal{S}$, but $\vec{E}_{inc}$ is not usually measured in $\mathcal{D}$ for the following reasons [47] :

1. Sampling for $\vec{E}_{inc}$ for a finely discretized $\mathcal{D}$ (usually smaller than $\frac{1}{10}\lambda$) would take a large amount of time.

2. Finely resolved measurements may not be possible due to the physical dimensions of currently available near-field probes, *e.g.* open-ended waveguides.

3. In order to be accurate, the measuring of $\vec{E}_{inc}$ in $\mathcal{D}$ would have to occur in the environment of operation, *i.e.* in the presence of the MWI apparatus with all the receivers and equipment in place which is difficult.

Due to the reasons above, inverse scattering algorithms often model the incident fields in $\mathcal{D}$ as being produced by simple sources such as line sources for 2D problems or point sources for 3D problems because the incident field distributions are known analytically [53]. In order to compensate for the error between the true incident field in $\mathcal{D}$, and the assumed incident field certain calibration techniques are used. These calibration techniques attempt to take the scattered field calculated from the measured data on $\mathcal{S}$ and create a new scattered dataset that would have existed if the true incident fields were replaced with those fields that were assumed for the model. This new calibrated scattered dataset, along with the simple source incident field in $\mathcal{D}$ is given to the inverse scattering algorithms for calculation of the dielectric profile of the OI. The two most used calibration techniques incident field and scattered field calibration (see [53]) are heuristic techniques, and can fail in certain cases as was shown in [53].

4.1.3 Using the Source Reconstruction Method to Calculate the Incident Field in $\mathcal{D}$

In this chapter we outline the idea of using the SRM to obtain the incident field in $\mathcal{D}$ for use in inverse scattering algorithms instead of using simple sources with the usual calibration methods. The general idea is that when one transmitter is on and all the other receivers are measuring the incident field on $\mathcal{S}$, we use the incident field on $\mathcal{S}$ as input to the SRM and solve for source currents that replace the radiating transmitter. The source currents are then used in a forward problem to estimate the incident field in $\mathcal{D}$ for that transmitter and this process is repeated for all the remaining transmitters. This idea is shown in Figure 4.2 where in the popular MWT configuration shown in Figure 4.1, the transmitter is replaced with equivalent sources on $\mathcal{S}'$ that we obtain from the measured data on S. The SRM calculated incident fields in $\mathcal{D}$ are then used along with the uncalibrated (raw) measured data as input to the inverse scattering algorithms to obtain the dielectric profile of the OI.

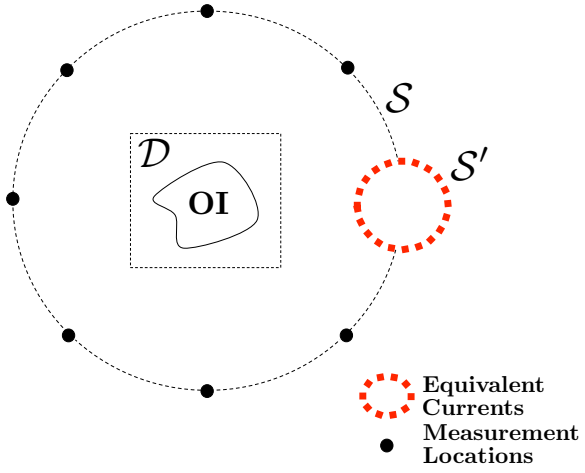

Figure 4.2: The SRM variation on the popular MWI configuration where the transmitter is replaced with equivalent sources on a reconstruction surface $\mathcal{S}'$ calculated from measured field values on $\mathcal{S}$. This apparatus is in the x-y plane.

The SRM seems suitable for this application because even though better results may be obtained with a full set of tangential field measurements sampled according to the operating frequency, we can still calculate incident field models with our limited dataset. This is useful because in problem configurations such as 2D transverse magnetic (TM) MWT only the component of the tangential field that is perpendicular to $\mathcal{D}$ is measured and no other tangential components. Transverse magnetic in this case, means that the magnetic field is parallel to the imaging domain $\mathcal{D}$ which is in the x-y plane. Consequently, the only electric field component is the one that is perpendicular to the x-y plane. The 2D TM MWT framework will be used to demonstrate our SRM method.

It should also be mentioned that when using the SRM the calculated equivalent currents are not unique (due to the ill-posedness of the inverse problem) but we can still obtain reasonable incident field estimates in $\mathcal{D}$ as will be shown in later sections.

4.1.3.1 The Source Reconstruction Method for 2D Transverse Magnetic Microwave Tomography

The SRM was applied to obtain the incident electric field estimates in the imaging domain $\mathcal{D}$ for 2D TM MWT problems. Once again we start from (2.1) to be able to map current sources on the reconstruction surface $\mathcal{S}'$ to the measured field values on $\mathcal{S}$. The assumption of a 2D TM MWT problem enables simplification of (2.1) because we are assuming only the z-component ($\mathcal{D}$ is in the x-y plane) of the electric field exists, and therefore only the z-component of the electric current exists. The mapping between the currents and measured z-component of the electric field is shown in (4.4) and was originally shown in [47]

$$
\begin{aligned}
E_z^{J_z}(\vec{r}) &= \frac{-\omega\mu_0}{4}\int_{\mathcal{S}'} J_z H_0^2(k_b|\vec{r}-\vec{r}\,'|)\,dl' \\
E_z^{M_x}(\vec{r}) &= \frac{-1}{4j}\int_{\mathcal{S}'} M_x k_b H_1^2(k_b|\vec{r}-\vec{r}\,'|)\frac{(y-y')}{|\vec{r}-\vec{r}\,'|}\,dl' \\
E_z^{M_y}(\vec{r}) &= \frac{1}{4j}\int_{\mathcal{S}'} M_y k_b H_1^2(k_b|\vec{r}-\vec{r}\,'|)\frac{(x-x')}{|\vec{r}-\vec{r}\,'|}\,dl'
\end{aligned}
\tag{4.4}
$$

Equation (4.4) shows three scalar equations. The first ($E_z^{J_z}(\vec{r})$) is the contribution to the electric field by the z-component of the electric current, the second and third ($E_z^{M_x}(\vec{r})$ and $E_z^{M_y}(\vec{r})$) show the contributions to the electric field by the x and y components of the magnetic current, respectively. The total electric field at a point on $\mathcal{S}$ can be calculated by summing these individual contributions. Furthermore, k_b is the background wavenumber of the medium, dl' bounds $\mathcal{S}'$, $\vec{r} \in \mathcal{S}$, and $\vec{r}\,' \in \mathcal{S}'$.

We expand the integrals in (4.4) assuming a simple pulse basis representation for the equivalent currents. Once discretized, we obtain our linear matrix equation (first shown in [47])

$$
\underbrace{\begin{bmatrix} \mathbf{A_{J_z}} & \mathbf{A_{M_x}} & \mathbf{A_{M_y}} \end{bmatrix}}_{\mathbf{A}}
\underbrace{\begin{bmatrix} \mathbf{J_z} \\ \mathbf{M_x} \\ \mathbf{M_y} \end{bmatrix}}_{\mathbf{x}}
= \underbrace{\mathbf{E_z}}_{\mathbf{b}}. \tag{4.5}
$$

In (4.5), $\mathbf{E_z}$ is a column vector containing the measured electric field values at the measurement locations. Operators $\mathbf{A_{J_z}}$, $\mathbf{A_{M_x}}$, and $\mathbf{A_{M_y}}$ are sub-matrices formed by discretizing the J_z, M_x, and M_y parts of (4.4) that act on the currents, respectively. Finally $\mathbf{J_z}$, $\mathbf{M_x}$, and $\mathbf{M_y}$ are column vectors containing the unknown current density coefficients for all the reconstruction circle points on $\mathcal{S}'$ (see Figure 4.2).

4.1.3.2 Source Reconstruction Method Inversion

We used CGLS to invert the system shown in (4.5) (see Section 2.2.2.2). To regularize this ill-posed problem, the CGLS iterations were terminated according to the L-curve technique as described in Section 2.2.2.3. The L^2-norms of the residual ($\mathbf{Ax} - \mathbf{b}$) and solution $\mathbf{x}$ were graphed for many iterations to ensure a full L-curve was present for the first transmitter in the MWT setup (see Figures 4.1 and 4.2). Then the iteration at the 'knee point' or corner of the L-curve was chosen as the solution iteration to balance the size of the residual and the size of the solution. The same iteration number was used to terminate CGLS for all the other transmitters in the MWT setup. This was done in the interest of simplicity with the assumption that the symmetry of the problem would produce similar L-curves. Once the current distribution was found for each transmitter, it was used in a forward problem to calculate the incident field in $\mathcal{D}$.

We note that our technique for regularizing the CGLS iterations is *ad hoc* as it requires choosing the knee point of the L-curve, but more robust methods for regularization can be studied in the future.

4.2 Results

The results of the implementation of the SRM to the 2D TM MWT problem are shown in this section. First it is synthetically shown that the SRM can produce accurate incident field models in $\mathcal{D}$, even with the limited measured data. Next, we use the SRM produced incident field models in $\mathcal{D}$ to calculate dielectric profiles of OIs using a previously developed MR-GNI algorithm. We first show images from synthetically generated measured data comparing the SRM method to images obtained using simple

incident field calibration. Then we show a similar comparison using experimental data for both lossless and lossy OIs.

4.2.1 Synthetic Results

This section shows results with synthetically generated measured data. Before showing any imaging results, it is demonstrated that the SRM can model the incident field in the imaging domain $\mathcal{D}$ even with the limited measured data available in a MWT setup.

4.2.1.1 Source Reconstruction Method Incident Field Estimation

For this test, consider an MWT apparatus similar to Figure 4.1 but with 24 transceivers on $\mathcal{S}$ in a circle of radius 13.54 cm. The true incident field will be modelled similar to [54] with at a frequency of 5 GHz

$$E_{\text{inc}}^{\text{true}}(\vec{r}) = \hat{z} \underbrace{\frac{1}{4j} H_0^2(k_b|\vec{r} - \vec{r}'|)}_{\text{line source}} \cos^m \zeta \tag{4.6}$$

where ζ is the angle between the transmitting antenna's boresight axis and the line connecting the transmitting antenna to the observation point (point we want to calculate the true incident field) $\vec{r}$, and k_b is the wavenumber of the background medium. This angle is shown in Figure 4.3. In (4.6) the parameter m is a positive integer that focuses the incident field; the greater m is, the more focused the field and the greater discrepancy from a line source.

We use the SRM to calculate $E_{\text{inc}}^{\text{SRM}}(\vec{r})$ where $\vec{r} \in \mathcal{D}$ from $E_{\text{inc}}^{\text{true}}(\vec{r})$ where $\vec{r} \in \mathcal{S}$. We also use (4.6) to calculate $E_{\text{inc}}^{\text{true}}(\vec{r})$ $\vec{r} \in \mathcal{D}$ for comparison. Figure 4.4 shows the SRM calculated incident field in $\mathcal{D}$, where the measured data was synthetically generated on

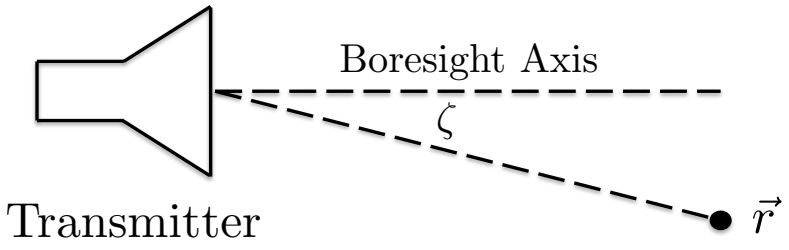

Figure 4.3: The angle ζ is the angle between the transmitter boresight axis and line connecting the transmitter to $\vec{r}$.

$\mathcal{S}$ from (4.6). The true incident field had a focusing level of $m = 2$. Figure 4.5 shows a similar comparison except $m = 5$. In this case there was also 2 % uniform white noise added to the measured data given as input to the SRM algorithm. This noise was calculated in the same way as in Section 3.2.1.

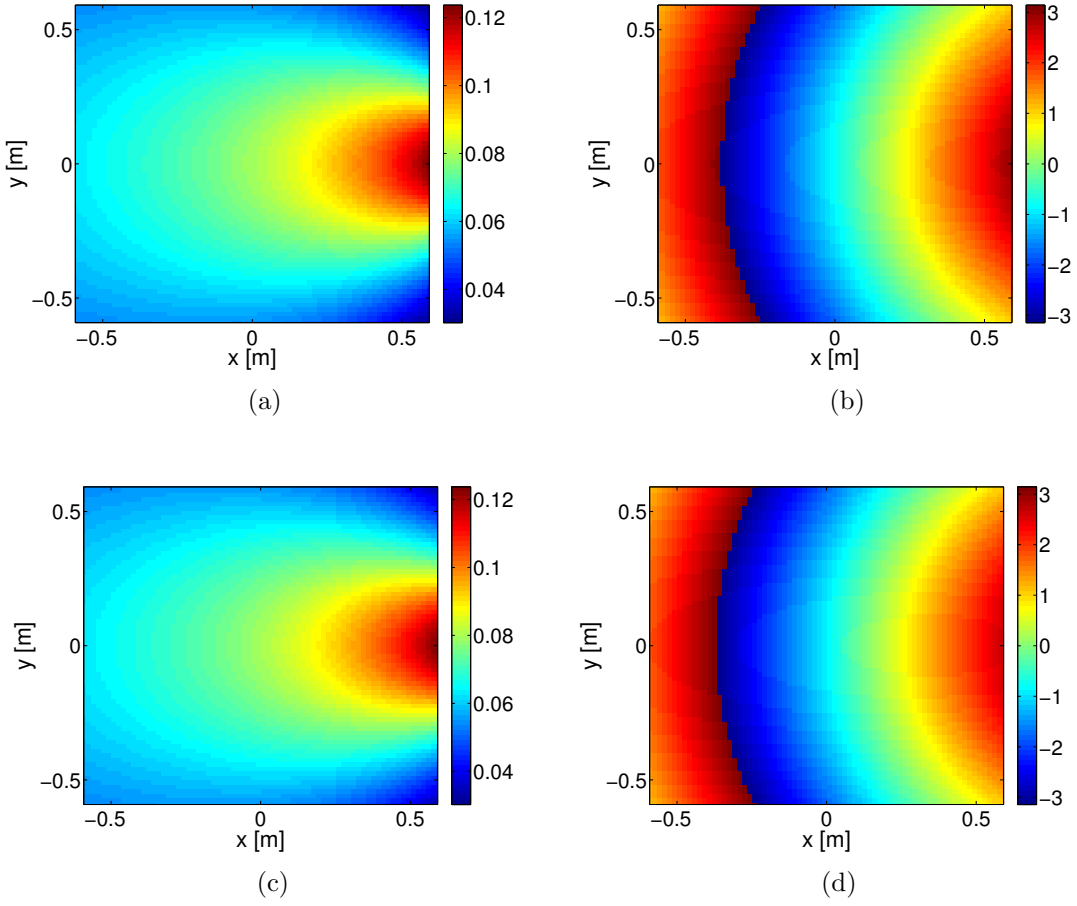

Figure 4.4: The true electric field E_{inc}^{true} [top] and SRM calculated electric field E_{inc}^{SRM} [bottom] in the imaging domain $\mathcal{D}$ for a focusing level of $m = 2$. The $|E_{inc}|$ is in $[V/m]$ [left] and $\angle E_{inc}$ is in $[rad]$ [right].

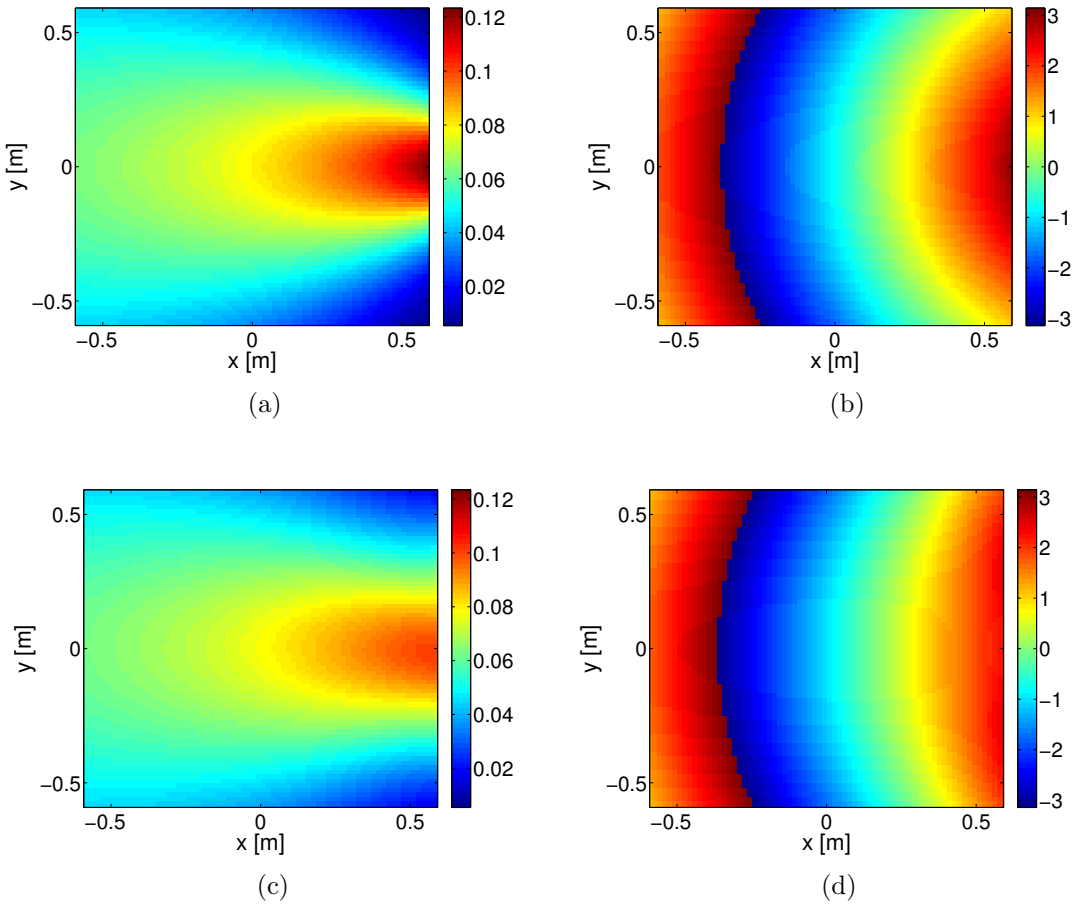

Figure 4.5: The true electric field E_{inc}^{true} [top] and SRM calculated electric field E_{inc}^{SRM} [bottom] in the imaging domain $\mathcal{D}$ for a focusing level of $m = 5$ and uniform white noise level of 2 % for the SRM measured data. The $|E_{inc}|$ is in $[V/m]$ [left] and $\angle E_{inc}$ is in $[rad]$ [right].

To compute the accuracy of the SRM we introduce η [%] which represents the normalized relative percent error calculated as in (4.7) and in [47] © 2011 IEEE. The norms (L^2 norms) were computed over the calculated incident field values in $\mathcal{D}$. A plot of η [%] over different focusing values m is shown in Figure 4.6 for different incident field estimation methods. We show the relative error using a line source to model the true field in $\mathcal{D}$, using the SRM with L-curve regularization, and using the SRM with L-curve regularization where 2 % uniform white noise was added to the generated measured data on $\mathcal{S}$.

$$\eta\ [\%] = \frac{\left\| E_{\text{true}}^{\text{inc}} - E_{\text{SRM}}^{\text{inc}} \right\|_{\mathcal{D}}}{\left\| E_{\text{true}}^{\text{inc}} \right\|_{\mathcal{D}}} \times 100\% \tag{4.7}$$

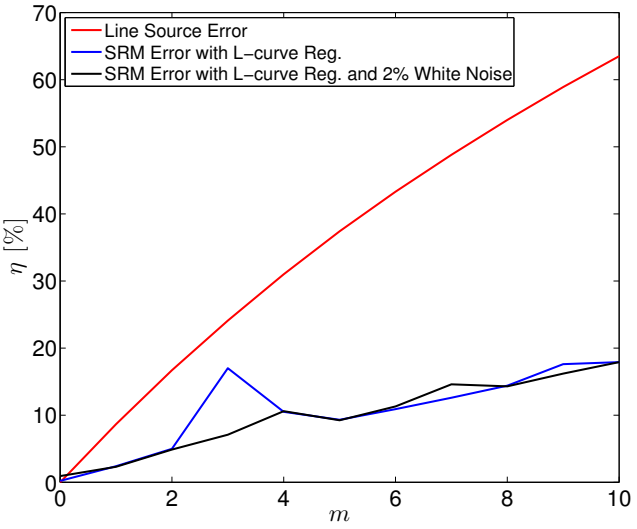

Figure 4.6: Normalized percent relative error $\eta[\%]$ for different incident field estimation methods for different focusing levels m: Line source [red], SRM calculated incident field with L-curve regularization [blue], and SRM calculated incident field with L-curve regularization and 2 % uniform white noise added to data on $\mathcal{S}$ [black]. © [2016] IEEE

We chose to test the SRM method with a true incident field that could be made more focused in $\mathcal{D}$, because it has been shown that making use of transmitters with a more focused near-field can lead to better images of the OI in MWT [54]. We can see from Figures 4.4 and 4.5 that even though we use measured data from 24 transmitters of only one tangential polarization, the SRM incident field estimates in $\mathcal{D}$ look very similar to the true fields.

Figure 4.6 confirms that the SRM is significantly better at modelling more focused fields than a line source, even with the limited measurement data that is available to calculate the equivalent currents. Consequently, the SRM may provide more flexibility in terms of the types of transmitters that are used in MWT. Currently, since simple sources (*e.g.* line sources) are most often used to model the incident field in $\mathcal{D}$, the larger the difference from a simple source, the more dependant MWT is on the heuristic calibration techniques mentioned earlier. SRM can provide more accurate incident field models, and

can be used along with raw measured data as input to inverse scattering algorithms.

4.2.1.2 Synthetic Microwave Tomography Results with Source Reconstruction Method Incident Fields

We will now show synthetically that the SRM can be used in conjunction with inverse scattering algorithms to produce accurate images of an OI.

Again we simulate a MWT setup similar to Figure 4.2, but with 32 transceivers equally spaced on a circle of 15 cm radius all operating at 7 GHz. We choose the true incident field distributions for these transmitters to be dictated by (4.6), with $m = 5$. The OI is assumed to be a lossless E-phantom originally used in [55] with a relative permittivity (ϵ_r) of 2.3. An image of the E-phantom can be seen in Figure 4.7 (a). We chose to use an E-phantom as our OI because the phantom's fingers vary in size and separation making it easy to spot differences when used for comparison with different imaging methods.

Using the above assumptions, measured data was synthesized for each transmitter at the receiver locations as in Figure 4.2. The appropriate receiver data was then used by the SRM to obtain equivalent current distributions, and subsequently to obtain the incident field estimates in $\mathcal{D}$ for each transmitter. We used these SRM incident field estimates, the true incident field in $\mathcal{D}$, and line source estimates (incident field in $\mathcal{D}$ is from a line source placed at the transmitter location) in separate tests with a pre-existing MR-GNI algorithm to image our synthetic OI. The real part of the image reconstruction is shown in Figure 4.7.

We can see by looking at Figure 4.7 that using the SRM estimated incident field performed comparably to using the true incident field in $\mathcal{D}$ in the image reconstruction of the OI. However, in the case of using the line source incident field with the MR-GNI

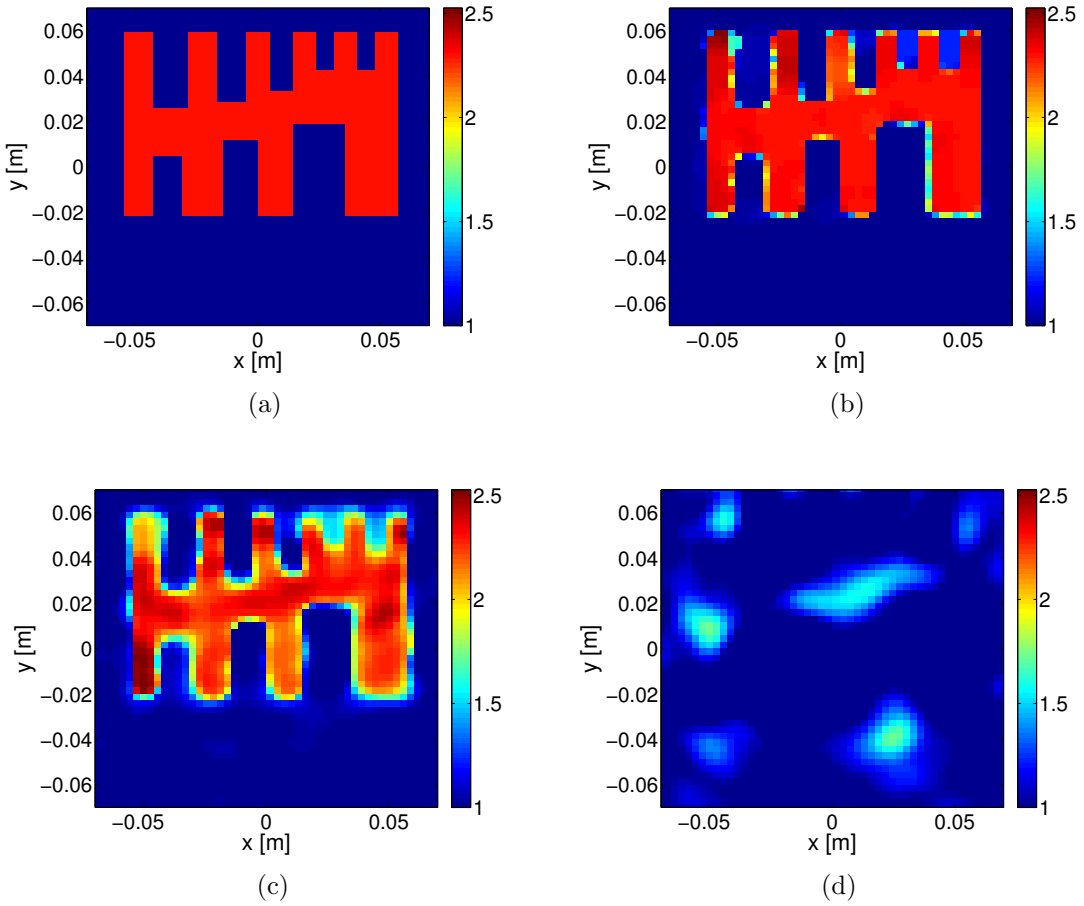

Figure 4.7: Synthetic imaging results of the reconstructed real part of the relative permittivity for an (a) E-phantom using different incident field estimates in $\mathcal{D}$ including: (b) The true incident field, (c) SRM calculated incident field, and (d) Line source incident field. © [2016] IEEE

algorithm, the image of the OI was unrecoverable. This shows that the SRM is producing incident field estimates that are accurate enough to be beneficial for inversion, even with the limited measurement data that is available with typical MWT configurations.

4.2.2 Experimental Results

Here we show that our SRM method works with raw experimental data collected at the MWT receivers. We compare our method by using the line source estimation for the incident field as well as simple incident field calibration. We use these datasets as inputs to the aforementioned MR-GNI algorithm.

4.2.2.1 Lossless Medium and Object of Interest

Experimental data was obtained from a 24 Vivaldi MWT system with an E-phantom as the OI with relative permittivity very close to $\epsilon_r = 2.3$ [56, 57][1]. This measured data was collected at 5, 7, and 8 GHz.

First the SRM was used to calculate the incident field in $\mathcal{D}$ for all transmitters. Since the true incident field is unknown for experimental tests, it is not possible to show the accuracy of the SRM calculated incident field in $\mathcal{D}$. Instead, a comparison of different incident fields obtained by different methods is shown on $\mathcal{S}$ in Figure 4.8. The SRM calculated incident field, the line source incident field, and the measured field are all shown at 5 and 8 GHz for one transmitter. The receiver indices in Figure 4.8 correspond to the different receivers around the imaging domain $\mathcal{D}$. The SRM incident fields closely follow the measured field magnitude and phase, while the line source incident field does not. The magnitude of the line source estimate is significantly different from the measured field.

Using the same MWT apparatus, we performed MR-GNI inversions with the incident field calculated via SRM and with the incident field from a line source. This was done for a frequency of 5 GHz, as well as 8 GHz using a frequency hopping technique [58]. In the frequency hopping method, we use the image obtained at 5GHz as an initial guess for 7 GHz (accounting for the increase in frequency) and then the 7 GHz image as an initial guess to obtain the image at 8 GHz. In the SRM case, we used raw (uncalibrated) measured data at the receivers whereas in the line source case, we used simple incident field calibration where the simulated incident field of the line source was matched to the

[1]Thank you to the Electromagnetic Imaging Laboratory at the University of Manitoba for providing the raw experimental data.

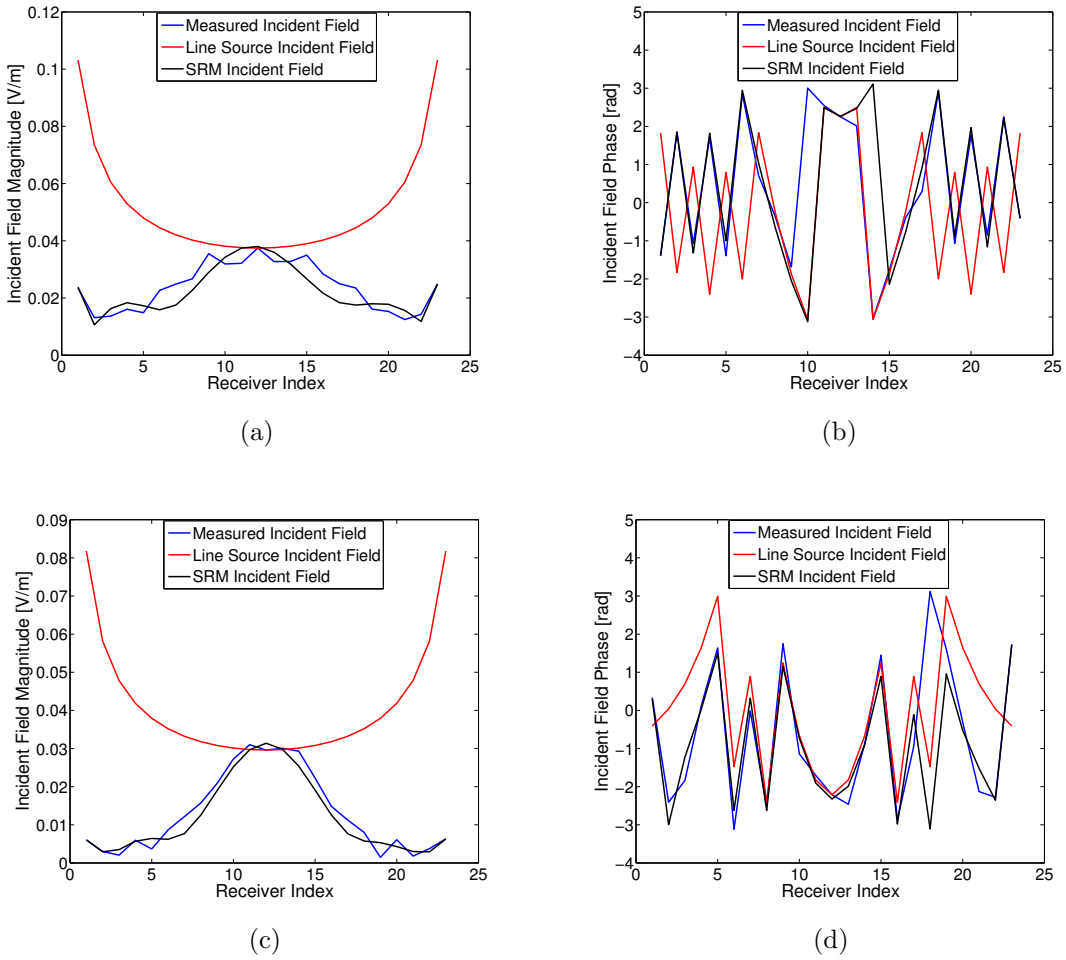

Figure 4.8: The electric field magnitude [left] and phase [right] at the receivers on $\mathcal{S}$ for a single transmitter for frequencies of 5 [top row] and 8 [bottom row] GHz. Figures (a) and (b) are © [2016] IEEE

measured incident field at the opposite receiver, *i.e.* the receiver directly in front of the transmitter. The results for this test are shown in Figure 4.9.

As can be seen from the 5 GHz reconstructions of Figure 4.9, both the SRM incident field estimate and line source estimate lead to reasonable reconstructions of the E-phantom, although it does seem like the line source case has more relative permittivity artifacts. In the frequency hopping case, we can see that the SRM incident field method was able to produce a much better reconstruction of the OI than the line source case. We speculate that this is due to the significant modelling error that is compounded at each new frequency step of the frequency hopping method. This is because at each new

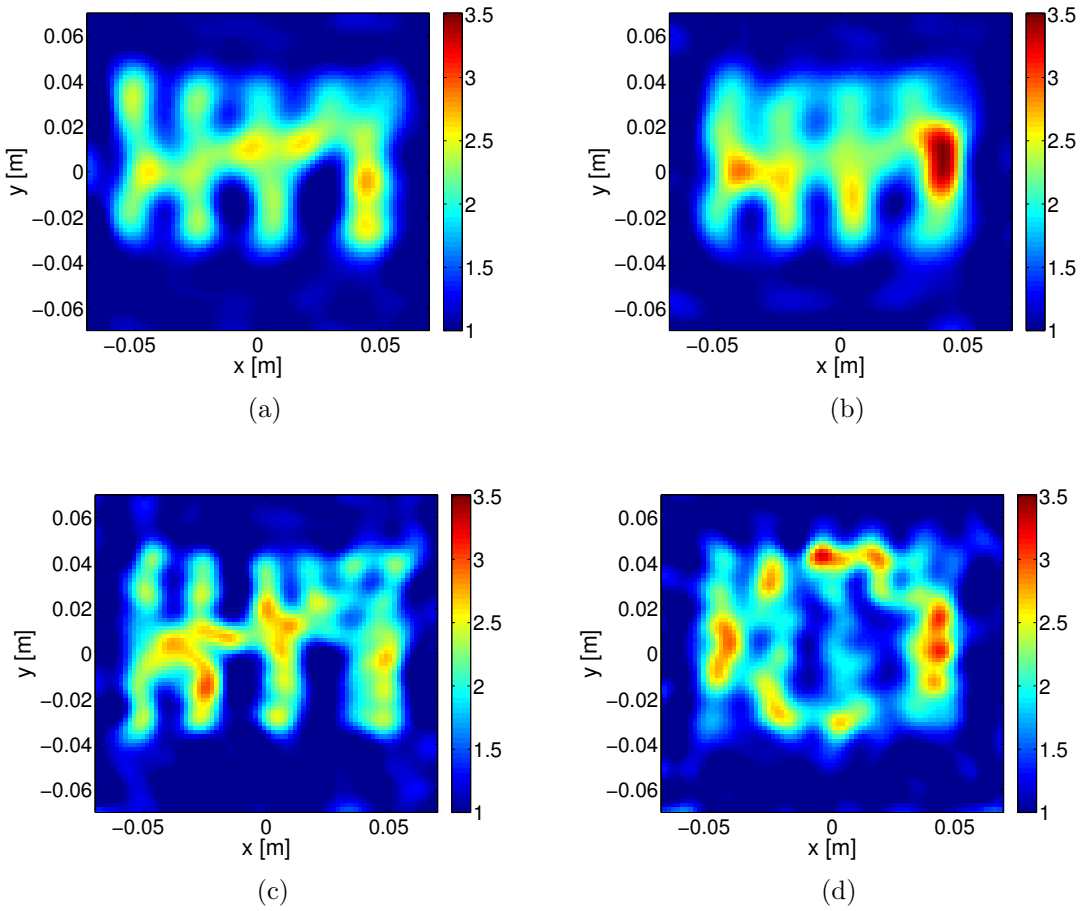

Figure 4.9: Reconstructed real part of the of the relative permittivity for an experimental E-phantom calculated by using the SRM incident field [left] and line source incident fields [right] with MR-GNI. Results are shown for a frequency of 5 GHz [top], and a frequency hopped case for a frequency of 8 GHz [bottom].

frequency we use the SRM to obtain a new incident field estimate from measured data at the receivers, which should serve to limit modelling error.

4.2.2.2 Lossy Medium and Object of Interest

In many cases, we may be interested in imaging in a lossy medium with a lossy OI *e.g.* biomedical imaging applications. Lossy background mediums are also often used to prevent mutual coupling effects between transmitters in the MWT apparatus. In this section, we show that our method works with lossy experiments as well.

To this end, experimental data from a 24-dipole antenna MWT system was collected for a skinless bovine leg (OI) immersed in a lossy saltwater medium of measured $\epsilon_r = 76 - 14j$ at a frequency of 0.8 GHz [59][2]. This data was used along with either the SRM produced incident field (calculated from raw data) or the line source incident field (along with the aforementioned simple incident field calibration) to reconstruct images of the skinless bovine leg using the MR-GNI algorithm.

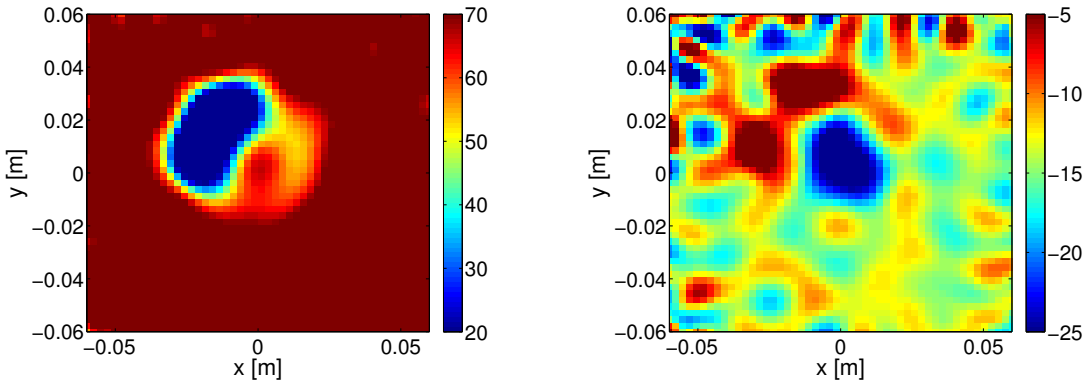

(a) (b)

Figure 4.10: Reconstructed real [left] and imaginary [right] parts of the relative complex permittivity of the skinless bovine leg calculated by using the SRM incident field in $\mathcal{D}$ with MR-GNI. Results are shown for a frequency of 0.8 GHz. The images produced with line source incident field estimates, and simple incident field calibration failed to produce meaningful results. © [2016] IEEE

The results for the SRM incident field reconstruction of the bovine leg is shown in Figure 4.10. The line source incident field reconstruction is not shown because it failed to produce a meaningful image of the skinless bovine leg.

The permittivity of the bovine leg was previously measured in [59, Table II], and images of the skinless bovine leg were obtained from an MR-GNI algorithm using scattered field calibration in [59, Figure 4]. When we compare the images in Figure 4.10 to those obtained in [59], we see good agreement.

[2]Thank you to Dr. Ostadrahimi and the Electromagnetic Imaging Laboratory at the University of Manitoba for providing the raw experimental data.

We have shown in this chapter that the SRM can be used along with inverse scattering algorithms to obtain accurate images of lossless and lossy OIs when compared with the currently available techniques. The SRM was able to calculate more accurate incident field models in $\mathcal{D}$ than the more traditional method of using a line source to model the incident field in $\mathcal{D}$. Using the SRM method does not require calibrated data to obtain meaningful images of the OI. Furthermore, we do not need any extra equipment in the MWT apparatus to perform this method.

Chapter 5

Conclusion

This thesis contributed to the study of antenna characterization by investigating and adding to the research about the Source Reconstructed Method (SRM) while reinforcing its flexibility.

First, a spherical SRM algorithm was implemented. The diagnostic capability of the SRM was shown synthetically and the implemented algorithm compared well to commercial modal expansion software in experimental testing. It was also experimentally demonstrated that equivalent currents can give meaningful information about the antenna under test. Experimental results also showed the ability of the SRM to calculate accurate far-field results with a partial measured field dataset.

Next, the issue of the added computational complexity of the SRM was addressed. The hierarchical matrix framework was investigated for use with the SRM and it was shown that it can reduce memory requirements and increase the speed of execution. The hierarchical matrix framework was shown to be most effective for use with SRM when Love's condition is in use.

Finally, the flexibility of the SRM was utilized in a novel approach to obtain incident field estimates in the imaging domain for microwave tomography. It was demonstrated through synthetic and experimental testing that this SRM incident field technique could be used with MR-GNI to obtain accurate images using raw uncalibrated measured data. The implemented technique requires no extra equipment not already present in the microwave tomography setup.

There are many future research avenues that can be taken from this thesis. In the short term we can expand the implemented algorithm to work with conformal reconstruction surfaces. It can then be investigated how close we can get to obtaining the true currents distribution of an antenna by perfecting robust regularization techniques and researching new methods of including prior information. In the long term this can be expanded to antenna design. We can explore the possibility of synthesizing field patterns to use as measured data, and use the SRM to characterize an antenna that can create that distribution. Creating such a general tool would be of great interest to the antenna industry.

Appendix A

Preliminary $\mathcal{H}$-matrix vs. MLFMM Comparison for use with SRM

Preliminary research was done on the comparison of using MLFMM vs. the $\mathcal{H}$-matrix framework for use with the SRM. MLFMM and the $\mathcal{H}$-matrix framework were used in conjunction with the SRM for two different problem sizes, and the problem setup and results and of these tests are shown in Figure A.1. Highly optimized MLFMM and $\mathcal{H}$-matrix algorithms were used for these tests[1].

The test cases where spherical SRM problems as described in Chapter 3, wherein Love's condition was enforced at points on a recessed mesh from the reconstruction surface. The RWG basis was used for the unknown equivalent currents. The amount of measurement

[1]Thanks to Jonatan Aronsson from CEMWorks (Winnipeg, MB) for running these tests and providing the test results.

points, Love's points, and approximate amount of unknowns (triangles in Surf Mesh multiplied by $\frac{3}{2}$ are shown at the top of Figure A.1.

	Small case	Large Case
Surf mesh	~2000 triangles	~8000 triangles
All measurement	10397 pts	20207 pts
Loves	3016 pts	12826 pts
Mesurement	7381 pts	7381 pts

	Initialization Time ("matrix fill time")	Matrix-vector Product Time	Memory (MB)
Small Case			
Dense Matrix	36.8s	0.10s	1080
H-Matrix (recompressed multi-level ACA)	16.8s	0.10s	370
MLFMA	2.54s	3.23s	130
Large Case			
Dense Matrix	262.4s	0.75s	3810
H-Matrix (recompressed multi-level ACA)	79.99s	0.35s	540
MLFMA	28.2s	9.66	300

Figure A.1: A comparison of the MLFMM on $\mathcal{H}$-matrix framework used with the SRM.

The differences in the two algorithms can most clearly be seen in the large test case. The MLFMM has a faster matrix fill time, but the $\mathcal{H}$-matrix framework has a much better matrix-vector product time. The MLFMM is also less memory intensive than the $\mathcal{H}$-matrix framework for this SRM test. Due to the fact that the total time to solve the inverse problem that arises from SRM is based on matrix build time *and* matrix-vector product time (due to the CGLS inversion process), it is more beneficial for the problem size and frequency shown here to use the $\mathcal{H}$-matrix framework. Note that as we scale the problem this may change in favour of the MLFMM.

Bibliography

[1] Y. Álvarez, F. Las-Heras, and M. R. Pino, "Reconstruction of equivalent currents distribution over arbitrary three-dimensional surfaces based on integral equation algorithms," *IEEE Transactions on Antennas and Propagation*, vol. 55, no. 12, pp. 3460–3468, 2007.

[2] G. E. Evans, "Antenna measurement techniques," *Norwood, MA, Artech House, Inc., 1990, 238 p.*, vol. 1, 1990.

[3] C. A. Balanis, *Antenna theory: analysis and design*. John Wiley & Sons, 2016.

[4] L. H. Hemming, *Electromagnetic anechoic chambers*. Wiley Interscience, 2002.

[5] A. Olver, "Compact antenna test ranges," in *Antennas and Propagation, 1991. ICAP 91., Seventh International Conference on (IEE)*. IET, 1991, pp. 99–108.

[6] E. F. Knott, *Radar cross section measurements*. Springer Science & Business Media, 2012.

[7] A. Yaghjian, "An overview of near-field antenna measurements," *IEEE Transactions on Antennas and Propagation*, vol. 34, no. 1, pp. 30–45, 1986.

[8] D. T. Paris, W. M. Leach, and E. B. Joy, "Basic theory of probe-compensated near-field measurements," *Antennas and Propagation, IEEE Transactions on*, vol. 26, no. 3, pp. 373–379, 1978.

[9] Y. Álvarez, F. Las-Heras, and M. R. Pino, "On the comparison between the spherical wave expansion and the sources reconstruction method," *IEEE Transactions on Antennas and Propagation*, vol. 56, no. 10, pp. 3337–3341, 2008.

[10] J. Hadamard, *Lectures on Cauchy's problem in linear partial differential equations*. Courier Corporation, 2014.

[11] S. Ponnapolli, "Near-field to far-field transformation utilizing the conjugate gradient method," *Application of Conjugate Gradient Method to Electromagnetics and Signal Analysis*, vol. 5, 1990.

[12] S. Ponnapalli, T. Sarkar, and P. Petre, "Near-field to far-field transformation using an equivalent current approach," in *Antennas and Propagation Society International Symposium, 1991. AP-S. Digest.* IEEE, 1991.

[13] P. Petre and T. K. Sarkar, "A planar near-field to far-field transformation using an equivalent magnetic current approach," in *Antennas and Propagation Society International Symposium, 1992. AP-S. 1992 Digest. Held in Conjuction with: URSI Radio Science Meeting and Nuclear EMP Meeting., IEEE.* IEEE, 1992, pp. 1534–1537.

[14] A. Taaghol and T. K. Sarkar, "Near-field to near/far-field transformation for arbitrary near-field geometry, utilizing an equivalent magnetic current," *IEEE Transactions on Electromagnetic Compatibility*, vol. 38, no. 3, pp. 536–542, 1996.

[15] T. K. Sarkar and A. Taaghol, "Near-field to near/far-field transformation for arbitrary near-field geometry utilizing an equivalent electric current and MoM," *IEEE Trans. Antennas Propag.*, vol. 47, no. 3, 1999.

[16] P. Petre and T. K. Sarkar, "Differences between modal expansion and intergral equation methods for planar near-field to far-field transformation," *Progress In Electromagnetics Research*, vol. 12, pp. 37–56, 1996.

[17] F. Las-Heras and T. K. Sarkar, "A direct optimization approach for source reconstruction and nf-ff transformation using amplitude-only data," *IEEE Transactions on Antennas and Propagation*, vol. 50, no. 4, pp. 500–510, 2002.

[18] F. Las-Heras, M. R. Pino, S. Loredo, Y. Alvarez, and T. K. Sarkar, "Evaluating near-field radiation patterns of commercial antennas," *IEEE Transactions on Antennas and Propagation*, vol. 54, no. 8, pp. 2198–2207, 2006.

[19] K. Persson and M. Gustafsson, "Reconstruction of equivalent currents using a near-field data transformation-with radome applications," *Progress In Electromagnetics Research*, vol. 54, pp. 179–198, 2005.

[20] Y. A. Lopez, F. Las-Heras Andres, M. R. Pino, and T. K. Sarkar, "An improved super-resolution source reconstruction method," *IEEE Trans. Instrum. Meas.*, vol. 58, no. 11, pp. 3855–3866, 2009.

[21] J. L. A. Quijano and G. Vecchi, "Improved-accuracy source reconstruction on arbitrary 3-D surfaces," *IEEE Antennas Wireless Propag. Lett.*, vol. 8, pp. 1046–1049, 2009.

[22] ——, "Field and source equivalence in source reconstruction on 3D surfaces," *Progress In Electromagnetics Research*, vol. 103, pp. 67–100, 2010.

[23] Y. Alvarez, F. Las-Heras, and M. R. Pino, "Probe-distortion correction for the sources reconstruction method," *IEEE Antennas and Propagation Magazine*, vol. 50, no. 6, pp. 117–124, 2008.

[24] Y. Lopez, F. Las-Heras, and M. Pino, "Application of the adaptive cross approximation algorithm to the sources reconstruction method," *EuCAP 2009*, 2009.

[25] T. F. Eibert and C. H. Schmidt, "Multilevel fast multipole accelerated inverse equivalent current method employing Rao–Wilton–Glisson discretization of electric and magnetic surface currents," *IEEE Transactions on Antennas and Propagation*, vol. 57, no. 4, pp. 1178–1185, 2009.

[26] T. F. Eibert, E. Kaliyaperumal, C. H. Schmidt *et al.*, "Inverse equivalent surface current method with hierarchical higher order basis functions, full probe correction and multilevel fast multipole acceleration," *Progress In Electromagnetics Research*, vol. 106, pp. 377–394, 2010.

[27] J. A. Lopez-Fernandez, M. Lopez-Portugues, Y. Alvarez-Lopez, C. Garcia-Gonzalez, D. Martínez, and F. Las Heras Andres, "Fast antenna characterization using the sources reconstruction method on graphics processors," *Progress In Electromagnetics Research*, vol. 126, pp. 185–201, 2012.

[28] N. Bayat, "On the role of antennas in the achievable resolution and accuracy from near-field microwave tomography," 2014.

[29] R. F. Harrington, *Time-harmonic electromagnetic fields*. McGraw-Hill, 1961.

[30] M. Oristaglio and H. Blok, "Wavefield imaging and inversion in electromagnetics and acoustics," *Course Notes TU Delft*, 1995.

[31] A. Devaney and G. Sherman, "Nonuniqueness in inverse source and scattering problems," *IEEE Transactions on Antennas and Propagation*, vol. 30, no. 5, pp. 1034–1037, 1982.

[32] P. C. Hansen, *Rank-deficient and discrete ill-posed problems: numerical aspects of linear inversion*. Siam, 1998, vol. 4.

[33] J. R. Shewchuk, "An introduction to the conjugate gradient method without the agonizing pain," 1994.

[34] P. C. Hansen, "Numerical tools for analysis and solution of fredholm integral equations of the first kind," *Inverse problems*, vol. 8, no. 6, p. 849, 1992.

[35] W. W. Hager and H. Zhang, "A survey of nonlinear conjugate gradient methods," *Pacific journal of Optimization*, vol. 2, no. 1, pp. 35–58, 2006.

[36] P. C. Hansen, "Regularization tools: A matlab package for analysis and solution of discrete ill-posed problems," *Numerical algorithms*, vol. 6, no. 1, pp. 1–35, 1994.

[37] S. Rao, D. Wilton, and A. Glisson, "Electromagnetic scattering by surfaces of arbitrary shape," *IEEE Transactions on antennas and propagation*, vol. 30, no. 3, pp. 409–418, 1982.

[38] C. Geuzaine and J.-F. Remacle, "Gmsh: A 3-D finite element mesh generator with built-in pre-and post-processing facilities," *International Journal for Numerical Methods in Engineering*, vol. 79, no. 11, pp. 1309–1331, 2009.

[39] Encyclopaedia of cubature formulas. [Online]. Available: http://nines.cs.kuleuven.be/research/ecf/ecf.html

[40] W. L. Stutzman, *Polarization in electromagnetic systems*. Artech house, 1993.

[41] Ö. Ergul and L. Gurel, "Efficient parallelization of the multilevel fast multipole algorithm for the solution of large-scale scattering problems," *IEEE Transactions on Antennas and Propagation*, vol. 56, no. 8, pp. 2335–2345, 2008.

[42] M. Bebendorf, *Hierarchical matrices*. Springer, 2008.

[43] K. Frederix and M. Van Barel, "Solving a large dense linear system by adaptive cross approximation," *Journal of computational and applied mathematics*, vol. 234, no. 11, pp. 3181–3195, 2010.

[44] E. Joy, *Near-field Antenna Measurement Techniques.* Georgia Tech Distance Learning and Professional Education, 2012.

[45] J. Song and W. C. Chew, "Multilevel fast-multipole algorithm for solving combined field integral equations of electromagnetic scattering," *Microwave and Optical Technology Letters*, vol. 10, no. 1, pp. 14–19, 1995.

[46] J. Song, C.-C. Lu, and W. C. Chew, "Multilevel fast multipole algorithm for electromagnetic scattering by large complex objects," *IEEE Transactions on Antennas and Propagation*, vol. 45, no. 10, pp. 1488–1493, 1997.

[47] C. Narendra, I. Jeffrey, and P. Mojabi, "Using the source reconstruction method to model incident fields in microwave tomography," *IEEE Antennas Wireless Propag. Lett.*, IEEE Early Access, 2016.

[48] M. Pastorino, *Microwave imaging.* John Wiley & Sons, 2010, vol. 208.

[49] A. Abubakar, T. Habashy, V. Druskin, L. Knizhnerman, and D. Alumbaugh, "2.5 D forward and inverse modeling for interpreting low-frequency electromagnetic measurements," *Geophysics*, vol. 73, no. 4, pp. F165–F177, 2008.

[50] P. Mojabi and J. LoVetri, "Microwave biomedical imaging using the multiplicative regularized Gauss-Newton inversion," *IEEE Antennas Wireless Propag. Lett.*, vol. 8, pp. 645–648, 2009.

[51] A. Abubakar, P. M. Van den Berg, and J. J. Mallorqui, "Imaging of biomedical data using a multiplicative regularized contrast source inversion method," *IEEE Transactions on Microwave Theory and Techniques*, vol. 50, no. 7, pp. 1761–1771, 2002.

[52] C. Gilmore, P. Mojabi, and J. LoVetri, "Comparison of an enhanced distorted Born iterative method and the multiplicative-regularized contrast source inversion method," *IEEE Trans. Antennas Propag.*, vol. 57, no. 8, pp. 2341–2351, 2009.

[53] M. Ostadrahimi et. al., "Analysis of incident field modeling and incident/scattered field calibration techniques in microwave tomography," *IEEE Antennas Wireless Propag. Lett.*, vol. 10, pp. 900–903, 2011.

[54] N. Bayat and P. Mojabi, "The effect of antenna incident field distribution on microwave tomography reconstruction," *Progress In Electromagnetics Research*, vol. 145, pp. 153–161, 2014.

[55] S. Y. Semenov, R. H. Svenson, A. E. Bulyshev, A. E. Souvorov, A. G. Nazarov, Y. E. Sizov, V. G. Posukh, A. V. Pavlovsky, P. N. Repin, and G. P. Tatsis, "Spatial resolution of microwave tomography for detection of myocardial ischemia and infarction-experimental study on two-dimensional models," *IEEE Trans. Microw. Theory Techn.*, vol. 48, no. 4, pp. 538–544, 2000.

[56] C. Gilmore, P. Mojabi, A. Zakaria, M. Ostadrahimi, C. Kaye, S. Noghanian, L. Shafai, S. Pistorius, and J. LoVetri, "A wideband microwave tomography system with a novel frequency selection procedure," *IEEE Trans. Biomed. Eng.*, vol. 57, no. 4, pp. 894–904, 2010.

[57] C. Gilmore, P. Mojabi, A. Zakaria, S. Pistorius, and J. LoVetri, "On super-resolution with an experimental microwave tomography system," *IEEE Antennas Wireless Propag. Lett.*, vol. 9, pp. 393–396, 2010.

[58] W. Chew and J. Lin, "A frequency-hopping approach for microwave imaging of large inhomogeneous bodies," *IEEE Microw. Guided Wave Lett.*, vol. 5, no. 12, pp. 439–441, 1995.

[59] M. Ostadrahimi, P. Mojabi, A. Zakaria, J. LoVetri, and L. Shafai, "Enhancement of Gauss-Newton inversion method for biological tissue imaging," *IEEE Transactions on Microwave Theory and Techniques*, vol. 61, no. 9, pp. 3424–3434, 2013.